T H E U N I V E R S I T Y O F T U L S A

THE GRADUATE SCHOOL

EXPERIMENTS, CFD SIMULATION AND MODELING OF FLUID VISCOSITY EFFECT IN ELECTRICAL SUBMERSIBLE PUMP

By
Zimo Lin

A thesis submitted in partial fulfillment of

the requirements for the degree of Master of Science

in the Discipline of Petroleum Engineering

The Graduate School

The University of Tulsa

2021

T H E U N I V E R S I T Y O F T U L S A

THE GRADUATE SCHOOL

EXPERIMENTS, CFD SIMULATION AND MODELING OF FLUID VISCOSITY EFFECT

IN ELECTRICAL SUBMERSIBLE PUMP

by
Zimo Lin

A THESIS

APPROVED FOR THE DISCIPLINE OF

PETROLEUM ENGINEERING

By Thesis Committee

Hong-Quan Zhang, Chair
Ovadia Shoham
Jun Lu
Haiwen Zhu

COPYRIGHT STATEMENT

ABSTRACT

Zimo Lin (Master of Science in Petroleum Engineering)

Experiments, CFD Simulation and Modeling of Fluid Viscosity Effect in Electrical Submersible Pump

Directed by Dr. Hong-Quan Zhang

79 pp, Chapter 5: Conclusions and Recommendations

(237 words)

A 12-stage mixed type electrical submersible pump (ESP), referred to as MTESP, was tested with single-phase water and industrial lubricate oil in a 2-inch closed flow loop. Experiments with different rotational speeds, different temperatures, and different flow rates were conducted and boosting pressure, temperature, and fluid volumetric flow rates were recorded during the test. Fluid viscosities up to 390 cP were tested with pump rotational speeds of 3600, 3000, and 2400 rpm. Oil viscosities changing with temperature were tested using rotary viscometer. As the viscosity increases, the ESP performance degrades.

Numerical simulation for two mixed-type ESPs, MTESP and DN1750, was conducted under viscous condition and validated with experimental results. The numerical simulation tends to overestimate the results in an acceptable range. ESP head performance from 1 cP to 1000 cP was obtained in numerical simulation to study the viscosity effect for the two pumps. The pump head curve is affected by fluid viscosity at low flow rates for mixed-type pumps was observed from numerical study.

An improved mechanistic model based on Euler equation is presented. The model predicts pump head performance for all fluid properties and pump types. A correlation for Euler head based on fluid viscosity and pump specific speed, and viscosity effect on turn loss is included in the improved model. The model results agree with the water and viscous fluid experiment data for two mixed-type pumps (MTESP and DN1750) and one radial-type pump TE2700.

ACKNOWLEDGEMENTS

First, I want to thank my advisor, Dr. Hong-Quan Zhang for accepting me to be his graduate student and gave me the opportunity as a research assistant of the Tulsa University Artificial Lift Projects (TUALP). Dr. Zhang's guidance and support not only helped me continue my academic career but also helped me correct my attitude towards life. His study on the environmental change of the Sahara also impresses me and I admire his tireless attitude toward scientific research.

I would like to thank the support from TUALP team. I want to give my special thanks to Dr. Haiwen Zhu, who helped me conduct experiments, using software, and gave me advice on doing research. I also want to thank Dr. Jianjun Zhu for help with learning CFD. I am grateful for the support given by Mr. Bryan Sams who helped me with building the experiment loop. Also, thanks to Ms. Donna Trankley who assisted purchasing the experiment components. I want to thank my TUALP team members: Qingqi Zhao, Jianlin Peng, Chengcheng Luo, Zhengjing Shen, Muhammad Rasyid Ridlah (Ridho), and Nursultan Bakyt for their help. I also want to thank my friends Qiuchen Wang, Shuyang Gao, Shihao Zhang and Yaxin Liu for giving me support for my research.

I wish to give my sincere appreciation to Dr. Ovadia Shoham and Dr. Jun Lu for being my thesis committee members.

At last, I am thankful for the huge support from my family. I want to thank my parents: Wei Lin and Wenbo Xu. Their unconditional love helps me through my lifetime.

TABLE OF CONTENTS

LIST OF FIGURES

LIST OF TABLES

INTRODUCTION

The electrical submersible pump (ESP) is a widely adopted artificial lift method that can provide outstanding profit for the petroleum industry, especially for the offshore fields. It can not only help sustain high flow rates but also create high boosting pressure for the production system. However, its performance is affected by the complicated downhole flow conditions. Therefore, attentions have been paid to the capability of ESP when handling high viscosity fluids in this study. The ESP is a composition of many centrifugal stages, which contains a rotating impeller, a static diffuser, sleeves, etc. The impeller is attached to the pump shaft, which is rotated by the submerged downhole motor. The blades on the rotational impeller provide kinetic energy on the fluid, which is transferred to the potential energy pressure in the diffuser vanes.

The ESP performance is affected by fluid properties, which makes the prediction of ESP performance under viscous flow important. Researchers performed centrifugal pump experiments with high viscosity fluids and established empirical correlations to predict the pump performance. However, most of those equations are limited to pump types, flow rate ranges, and viscosity ranges. On the other hand, the numerical simulation method, which is derived based on Navier-Stokes equations, can be used to predict the pump performance for any type of fluid and flow conditions. The results help understand the details of fluid behavior inside the stages. Based on the analysis from both methods, the mechanistic model, which is efficient and reliable, is developed for predicting ESP head performance under different flow conditions for all types of the pump.

Following the research methodology introduced above, this study firstly conducted single-phase water and oil ESP experiments. Then, the numerical simulation is performed and validated by the experiment to analyze the viscous flow behavior in ESP. Finally, the improved mechanistic model is presented and validated with experimental results.

CHAPTER 1

LITERATURE REVIEW

In this chapter, previous studies and experiments of viscous effects on ESP performance are discussed.

1.1 Ippen

Ippen (1946) conducted over 220 pump performance tests for oil viscosities from water to 10000 Saybolt second universal (SSU), which is about 1800 cP. Four different specifications of centrifugal pumps were tested by using different geometry of the impeller. The experiments covered a range of specific speeds between 1000 and 3000 due to different impeller shapes for each pump. Three types of oil were used to provide a large window of fluid viscosity. The pump head, capacity and input power characteristics influenced by viscosity changes and pump types were discussed. The pump number and specific speed of the pump are shown in Table 1.1.

Table 1.1 Specific speed of the pumps

Pump Number	Specific Speed for Water
IL 11	1163
IL 12	1163
IL 21	2622
IL 22	1991

Viscous losses in centrifugal pumps are analyzed, which are hydraulic losses, disk friction, ring losses and miscellaneous. Ring loss and disk friction were especially discussed. Two losses are introduced in ring loss, leakage losses and torque losses. Pump designer used to focus on leakage losses instead of torque losses. Because of the viscosity fluid are 10 to 2000 times more viscous than water, torque losses due to tangential shear created by the rotation of pump ring is an important factor.

The experiment results include head change and efficiency change with discharge flowrate in variance of viscosity. Also, the ratio of oil head to water head, ratio of oil brake horsepower (BHP) input to the water BHP input corrected by specific gravity and efficiency loss were plotted against Reynolds number. The Reynold number is defined as

$$R_D = 2620 \frac{Nd^2}{v * 10^5} \tag{1.1}$$

where *N* is the rotational speed of the impeller in rpm, *d* is the impeller diameter in ft, and *v* is the kinematic viscosity in centistokes.

The head and efficiency curve for different pumps and viscosities is presented in Figure 1.1. The performance curve of pump IL 11 with specific speed of 1163 and the rotational speed of 2875 is plotted on the left side. And the performance curve of pump IL 21 with specific speed of 2622 and the rotational speed of 1895 is plotted on the right side. In both pumps, head and efficiency curves fall with increase of the fluid viscosity. However, from the trend line of the head curve, it can be seen that the head will not decrease due to the viscosity change for pump IL 11, but head decreases with viscosity increases for pump IL 21 at flow rate starting point.

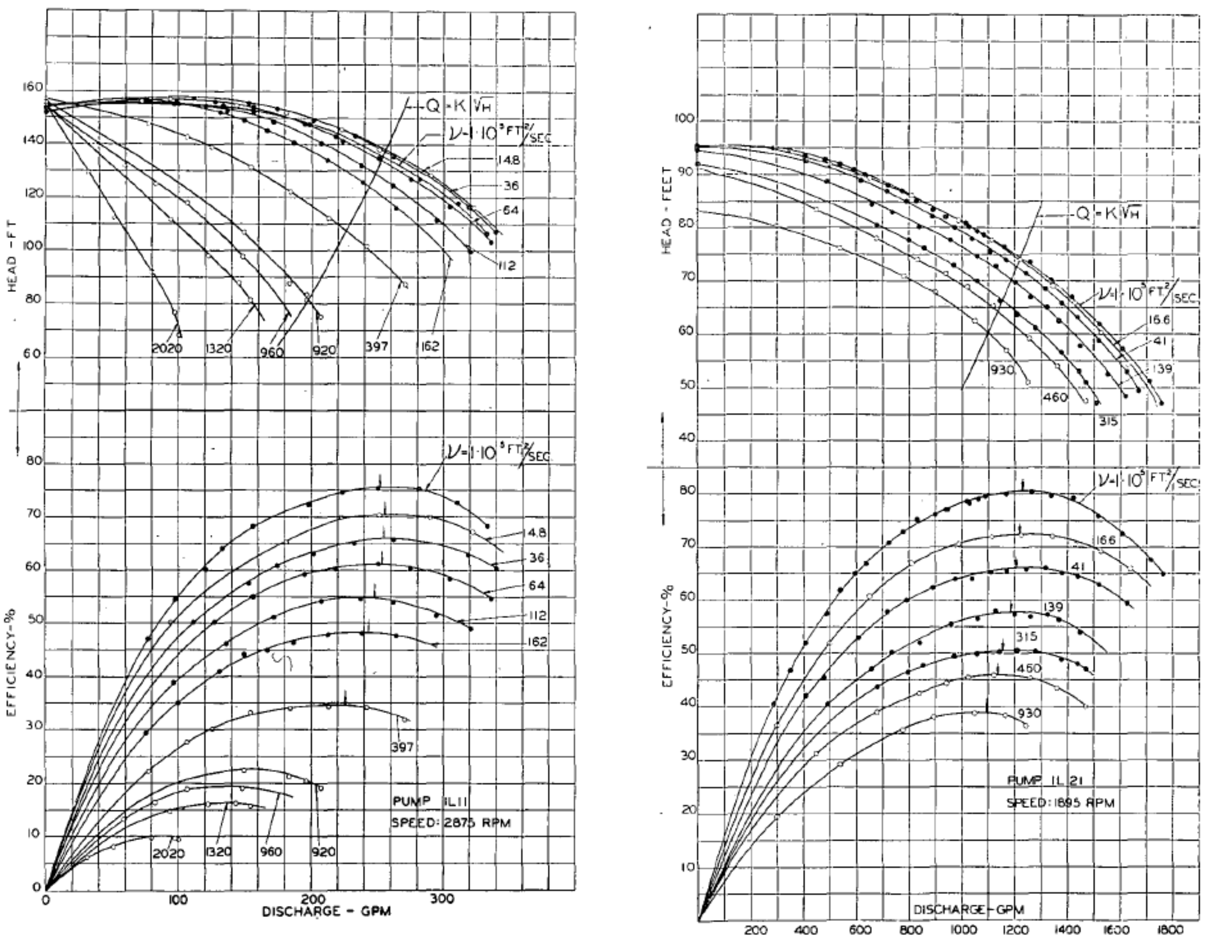

Figure 1.1 Head and efficiency curves for various pumps and viscosities (Ippen)

1.2 Stepanoff

Stepanoff (1949) conducted experiments using centrifugal pumps with fluid viscosities up to 2000 cSt. A dimensionless number pump specific speed was used in the study. Pump specific number is a classifier of pump impellers based on the impeller's shape and size.

The pump specific speed is calculated at the best efficiency point, which is

$$Ns = \frac{N\sqrt{q}}{H^{0.75}g^{0.75}} \tag{1.2}$$

where N is the rotational speed (rpm), q is the flow rate (gpm) and H is the pump head (ft). Nowadays, ESP manufacturers use a simplified equation:

$$Ns = \frac{N\sqrt{q}}{H^{0.75}} \tag{1.3}$$

where N is the rotational speed (rpm), q is the flow rate (gpm) at best efficiency point (BEP) and H is the pump head (ft) at BEP.

Stepanoff points out that the specific speed of pump should not change with the fluid viscosity, at the constant rotational speed the equation is shown below

$$\frac{q_{bep}^{vis}}{q_{bep}^{water}} = \left(\frac{H_{bep}^{vis}}{H_{bep}^{water}}\right)^{1.5} \tag{1.4}$$

where q_{bep}^{water} is the water flow rate at the BEP in gpm, q_{bep}^{vis} is the viscous fluid flow rate at the BEP in gpm, H_{bep}^{water} is the water head at the BEP in ft, and H_{bep}^{vis} is the viscous fluid head at the BEP in ft.

The flow rate correction factor is defined as

$$F_q = \frac{q_{bep}^{\mathrm{vis}}}{q_{\mathrm{bep}}^{\mathrm{water}}} \tag{1.5}$$

The head correction factor is defined as

$$F_H = \frac{H_{bep}^{vis}}{H_{bep}^{\mathrm{water}}} \tag{1.6}$$

Using these correction factors, the Eq. 1.4 can be rewritten as

$$F_q = (F_H)^{1.5} \tag{1.7}$$

The correction provides a simpler way to predict pump head performance under any viscous conditions if the water conditions are known at the same rotational speed.

Based on experiments, a new Reynold number Stepanoff Reynold number is defined as

$$R_{\mathrm{Stepanoff}} = 6.0345 \frac{N q_{\mathrm{bep}}^{\mathrm{vis}}}{\sqrt{H_{\mathrm{bep}}^{\mathrm{water}}}\, \nu} \tag{1.8}$$

where *v* is the kinematic liquid viscosity in cSt, *N* is the rotational speed in rpm, q_{bep}^{vis} is the pump flow rate for viscous fluid at best efficiency point in bpd, H_{bep}^{water} is the water head at best efficiency point in ft.

In Figure 1.2, the correction factors are plotted against Stepanoff Reynold number. The test pumps have the specific speed from 775 to 1980.

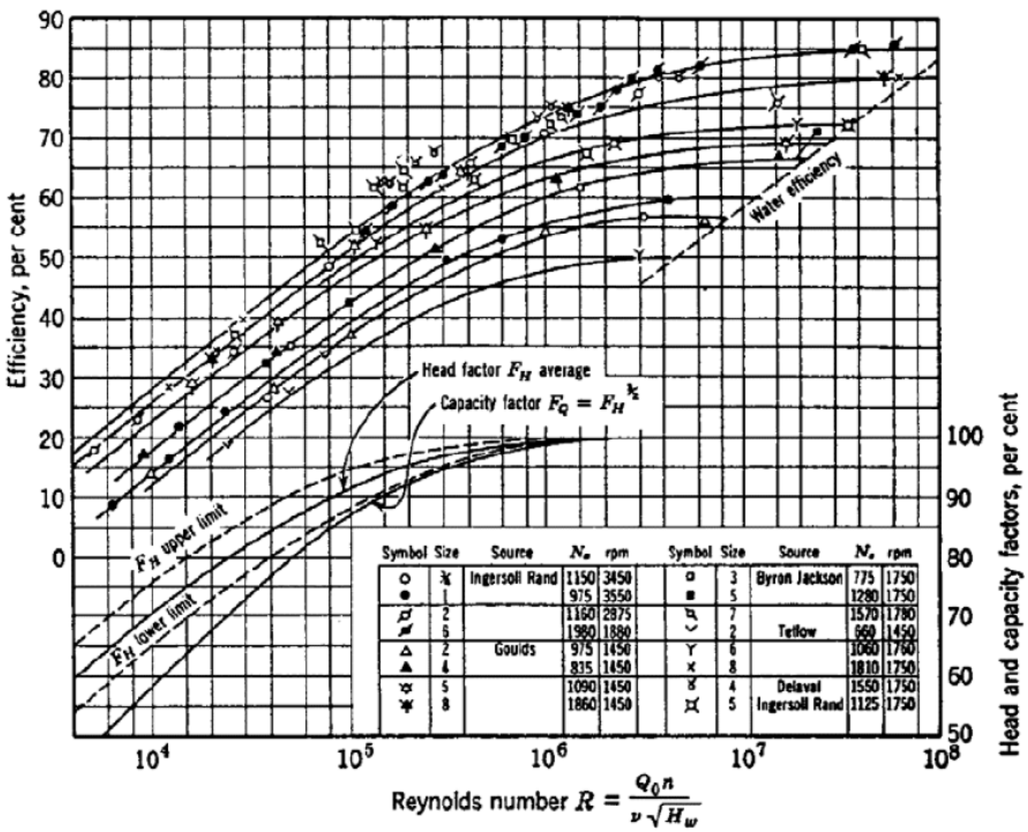

Figure 1.2 Head and efficiency corrections factors for different viscosity at BEP (Stepanoff)

Zhu (2017) mentioned that, with the different design and structure of impeller shrouds, hub and vanes of the ESP stage, flow direction at the impeller part changes, and ESPs can be categorized into radial, mixed, and axial type based on the flow path. The dimensionless factor specific speed (*Ns*) can give an identification of what type the ESP is. The pump is more radial for low *Ns* number which usually less than 1800, and it is more axial for high *Ns* number. The comparison of pump specific speeds is showing in Figure 1.3.

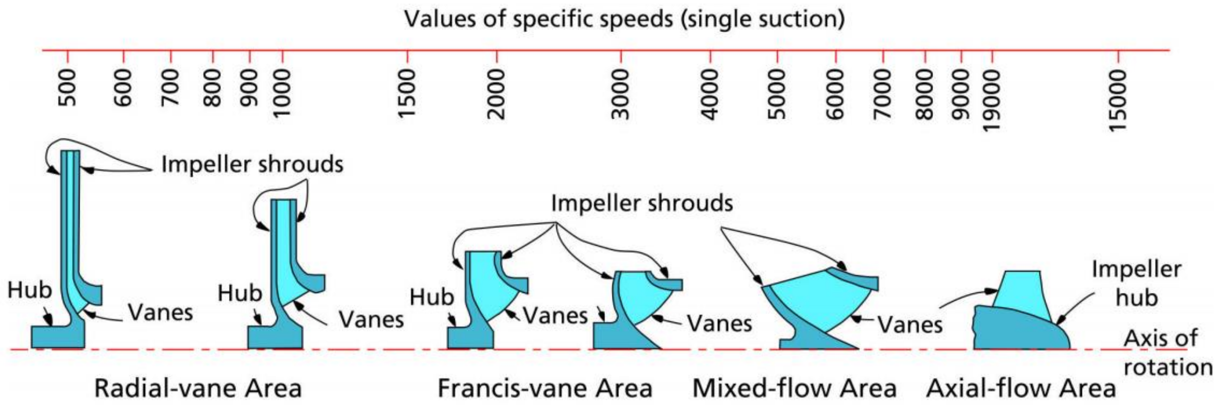

Figure 1.3 Comparison of pump specific speeds
(https://www.pumpfundamentals.com)

1.3 Amaral et al.

Amaral et al. (2009) tests two different centrifugal pumps with 1 cP water and 67 to 1020 cP clear glycerin. The first pump is a conventional radial two impeller ITA 65-300/2 pump with the specific speed of *Ns* = 1000, and the second pump is a semi-axial GN-7000 ESP which the specific speed *Ns* = 3850. In radial pump experiment, the rotational speed is around 910 rpm for semi-axial pump, the rotational speed is 3500 rpm. Head vs. flow rate curves of these two pumps were plotted and compared in the study. From the experiment result, in full range of operations, head reduction from 1 to 60 cP fluid viscosity is higher than 270 to 720 cP fluid viscosity. Amaral et al. point out the influences of fluid viscosity is depending on pump characteristics.

1.4 Sirino et al.

Sirino et al. (2013) used numerical analysis method to analyze viscosity influence on a semi-axial pump GN-7000. In the study, viscous fluid from 60 cP to 1020 cP was assumed for

CFD simulation and different flow rates and impeller speed were used. Single stage of the ESP including one impeller and one diffuser was simulated. Long intake pipe and discharge pipe were added at impeller inlet and diffuser outlet to improve numerical calculation. Balancing holes, casing clearances and leakage flow were neglected. For fluid viscosity 270 cP or higher, no turbulence models were used because the Reynolds number was lower than 1000 and flow was treated laminar flow in all regions. For other cases which had higher Reynolds numbers, turbulence model Shear Stress Transport (SST) model was used for consistency.

The numerical results agree with the experiment data and the deviations are less than 15% in pressure differences between impeller and diffuser. Numerical hydraulic efficiency was over predicted because leakage and clearances effects were neglected in the simulations. The overall trend and BEP match manufacturer catalog curve.

1.5 Barrios et al.

Barrios et al. (2012) used two ESP configurations to test ESP gas handling ability. A Multi-Vane Pump MVP 875 series G470 combined with mixed type ESP WJE1000 was compared with only WJE1000 pump configuration. Both single phase viscous flow test results and two-phase viscous flow were discussed and analyzed. For single phase flow, these two pumps were tested in manufacturer test facility. WJE1000 pump was test at 2625 rpm with fluid viscosity up to 2500 cP, and MVP-G470 pump was test at 3500 rpm with fluid viscosity up to 1000 cP. Head performance curve was plotted against flowrate for both pumps. For single phase WJE1000 pump, the head at very low flow rate decreases with increases of viscosity, and the performance trend curve are not converged at 0 flow rate. From 1 cP to 995 cP liquid viscosity, the head decreases approximately 20% at low flow rate region.

CHAPTER 2

EXPERIMENTAL SETUP AND RESULTS

This chapter presents the detailed information about the experimental facility, experimental program and experiment results for testing ESP under single phase water and oil flow conditions. The flow loop, ESP configurations, and data acquisition system (DAQ) are demonstrated in the Experimental Facility section below.

2.1 Experimental Facility

The experimental facility is upgraded from a previous gas-liquid-solid three phase flow loop which was constructed by Zhu (2019) to test sand erosion effect on MTESP. The schematic of the facility is shown in Figure 2.1 and the flow loop image is shown in Figure 2.2.A water tank, a fully closed flow loop, a gas injection system and a separator are the key components of the facility. This flow loop was used for testing ESP performance under water, gas, and sand conditions. An oil inlet is installed on the separator for adding high viscosity oil and oil level observation to perform the single-phase oil operation, as shown in Figure 2.3. The flow loop can perform fluid flowrates from 0 to 5000 bpd with fluid viscosity from 1 to 500 cp. The detailed experimental equipment and other major components used in this flow loop are listed in Appendix A.

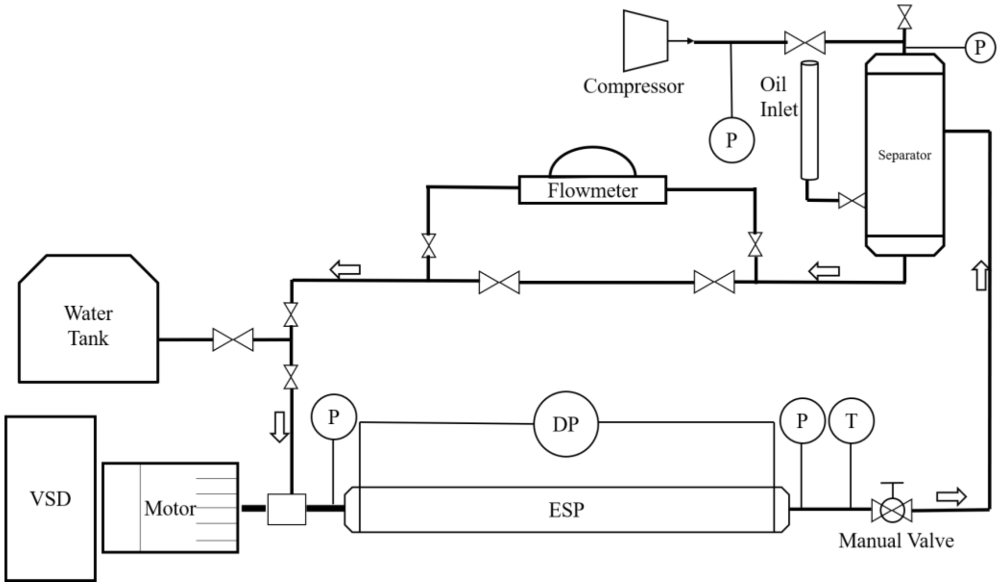

Figure 2.1 Schematic of TUALP single-phase oil ESP flow loop

Figure 2.2 Photo of TUALP single-phase oil ESP flow loop

Figure 2.3 Port for oil input

2.1.1 Single phase viscous fluid flow loop

As shown in Figure 2.1, the test facility consists of a 34-foot long 2-inch diameter steel pipe main flow loop connecting the testing ESP, a vertical separator, and a water tank. When the water test is performed, water is filled from water tank. When oil test is performed, oil is injected from the oil input port at the separator. An air compressor (Kaeser CSD60) connected to the separator was used for pressurizing the loop during the pump operation and a gas control valve (Emerson 24588SB) was used for regulating gas pressure. The loop maximum pressure is 200 psig and during the experiment, separator pressure was set to be fixed at 50 psig to give a constant inlet pressure to ESP and avoid pump cavitation problem which could cause damage. In the single-phase oil test and water test, most of the gas was separated by the separator and the gas void fraction was less than 1% during the operation. As shown in Figure 2.3, the oil input port on the separator was made of 4-inch and 2-inch diameter transparent PVC pipe for injecting oil into the loop. The oil column is an indicator that shows the liquid level inside separator. The liquid level in separator needs to be higher than the liquid inlet from the loop to avoid gas bubble entrainment into the ESP.

A manual gate valve controls flowrate at downstream of the loop after the ESP outlet. Then, fluid passes through the separator and flows through the Coriolis flowmeter which tracks the real time flowrate. A bypass line under the flowmeter was used for protection and it is closed during the pump testing of this study. The variable speed drive (FUJI ELECTRIC FRN050G1S-4U) controls the ESP rotational speed by activating the electric motor (WEG 05036EG3E326TS-W22). A torque sensor (S.Himmelstein model 721) was installed for monitoring the real rotational speed and pump torque. Eight differential pressure transmitters (Endress Hauser PMD75) on ESP measure the pressure difference between single pump stages, and absolute pressure transmitters were set before pump inlet and after pump outlet to monitor the total boosting pressure of the ESP. Type J Thermocouple with probe and a temperature transmitter (INOR IPAQ R330) was installed after the pump outlet to record fluid temperature with time inside the loop.

2.1.2 ESP configuration

At ESP testing bench, a motor, thrust chamber and other equipment are installed for ESP normal operation. The testing MTESP is a 12-stage mixed type 4-inch outer diameter multi-stage centrifugal pump. Its best efficiency point (BEP) is flowrate equal to 3100 bpd at 3600 rpm, and the boosting pressure at this point is 9.8 psig per stage. All 12 pump stages consist of the same type of impellers and diffusers. The diffusers' bore was made of special carbide material, this material provides higher hardness than general stages. As shown in Figure 2.4 (a), 8 differential pressure transmitters are connected to the ports on the pump housing to measure the pressures at 4 different single stages of the pump, namely stages 3, 6, 9 and 12. Quarter-inch holes were drilled on the pump housing and drilled on the designated stage diffuser grooves to create pressure communication between fluid inside the stage and the pressure transmitter outside the housing as shown in Figures 2.4 (b) and (c). To avoid stage to stage connection between housing and diffuser, Teflon O-rings were installed on the diffusers.

(a)

(b)

(c)

Figure 2.4 ESP components (a) ESP housing with pressure measurement ports, (b) Drilled hole on diffuser groove, (c) Drilled hole on ESP housing

Based on the pump catalog curve and the affinity law, pump head and efficiency curves at different rotational speeds can be predicted and plotted. The pump head decreases with liquid flowrate increase at the same rotational speed.

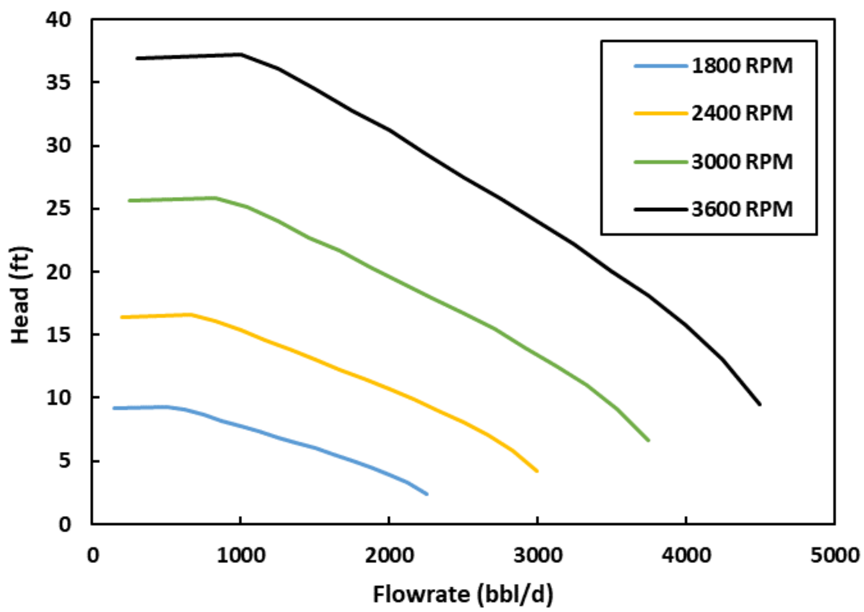

Figure 2.5 MTESP single stage water performance curve

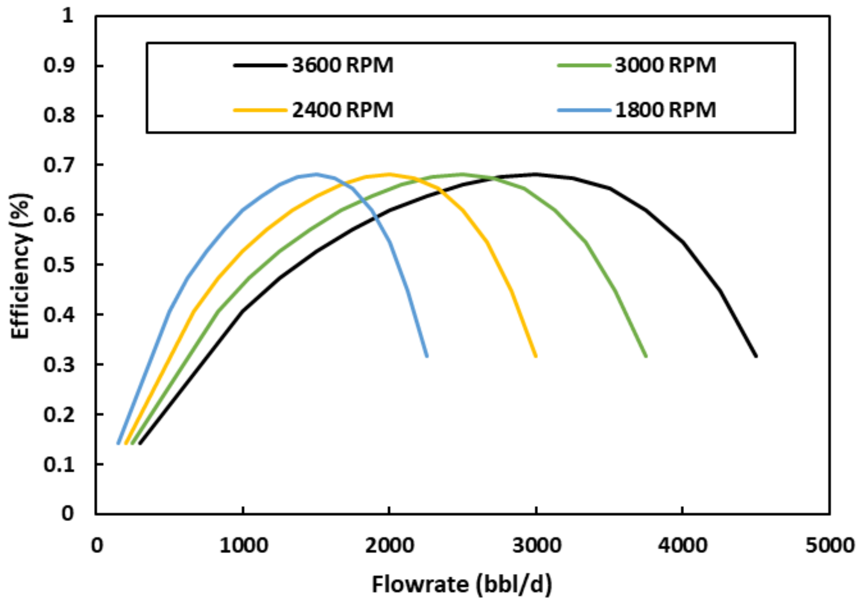

Figure 2.6 MTESP efficiency curves

The affinity law (Stepanoff, 1957) is

$$\frac{Q_1}{Q_2} = \frac{N_1}{N_2} \tag{2.1}$$

$$\frac{H_1}{H_2} = \left(\frac{N_1}{N_2}\right)^2 \tag{2.2}$$

$$\frac{BHP_1}{BHP_2} = \left(\frac{N_1}{N_2}\right)^3 \tag{2.3}$$

where Q is flow rate in bpd, N is rotational speed in rpm, H is hydraulic head in ft, and BHP is brake horsepower.

2.1.3 Data Acquisition System

This data acquisition system installed for the loop was programed using FieldPoint modules from National Instrument (NI) by Zhu (2019). NI Input module NI 9208 collect signal from pressure transmitters, temperature transmitter and flowmeter with a range of 4~20 mA. The NI output module NI 9265 releases internal control signals (4~20 mA) to control VSD and control valves. The input module NI 9228 connects to the torque sensor and provides high updating frequency. Graphical programing language Labview was used for constructing the DAQ program as shown in Figure 2.7. Signals can be received and recorded by connecting the NI modules to the computer that running DAQ program, all signals were converted to the field units and exported into data files. The detailed list of equipment in DAQ system are provided in Appendix A.

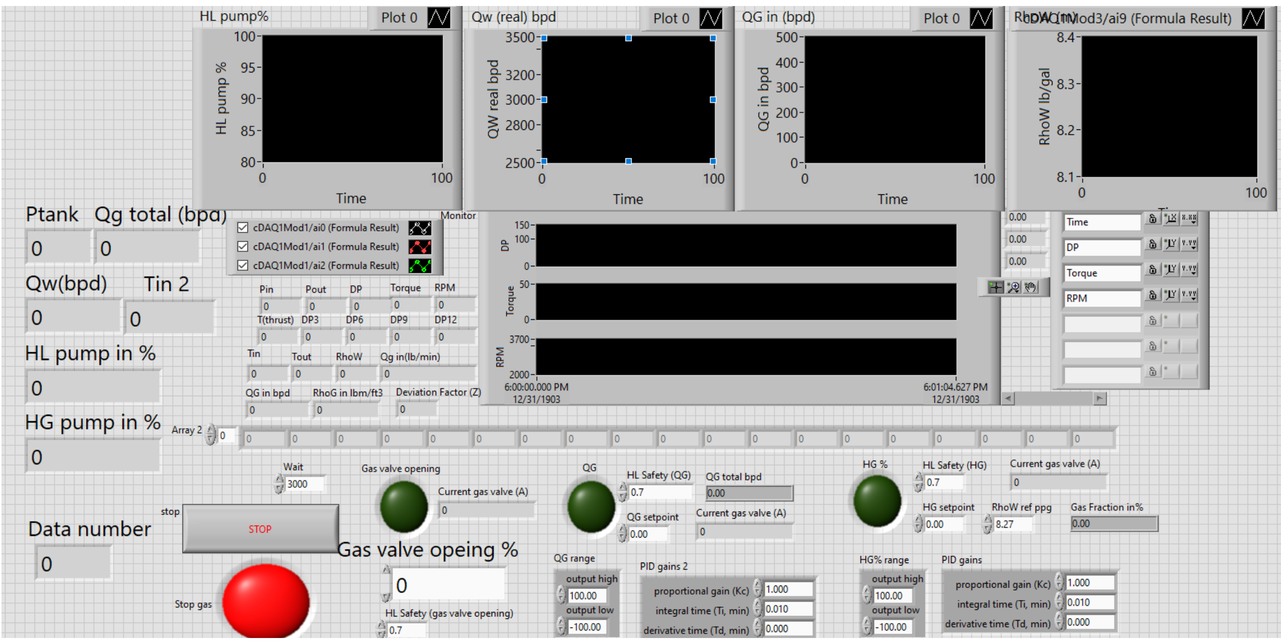

Figure 2.7 Data acquisition panel of TUALP single-phase oil ESP flow loop

2.2 Experimental Program

2.2.1 Test Fluids

The working fluids used in the experiments are tap water and industrial lubricating oil ISO-VG320. The oil viscosity was obtained using rotational rheometer (Anton Paar RheolabQC) with different temperatures. A water bath system (Julabo F-25 and Julabo MA) was used for maintaining the fluid temperature at the same level when measuring the fluid viscosity. Oil viscosity versus temperature is shown in Figure 2.8. The oil has a viscosity range of 1145 cP to 93 cP from 20 to 60 degree Celsius. At the same temperature, different shear stresses acting on the oil result in same viscosity, as shown in Figure 2.9, indicating Newtonian behavior. Density of the oil was provided by industry catalog that is 0.891 g/cm^3.

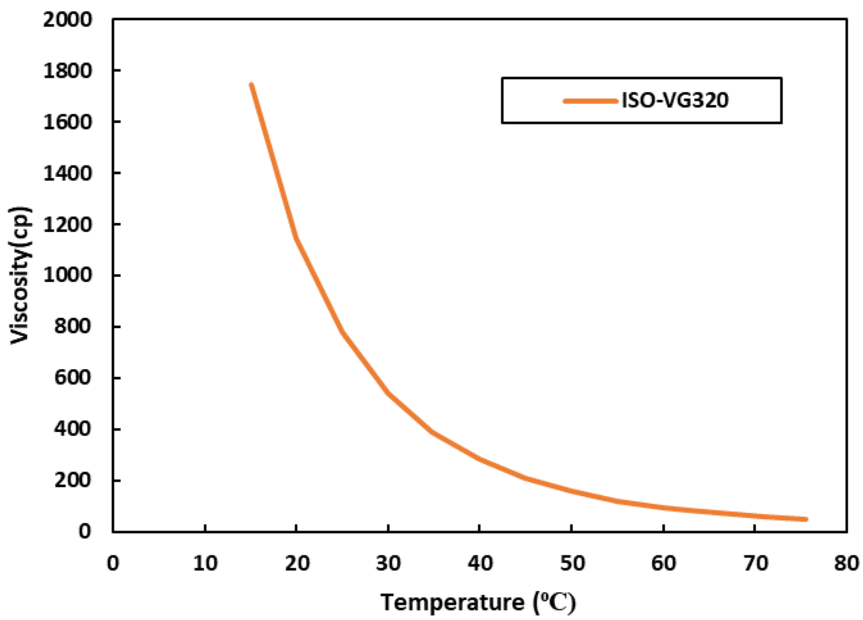

Figure 2.8 ISO-VG320 viscosity versus temperature

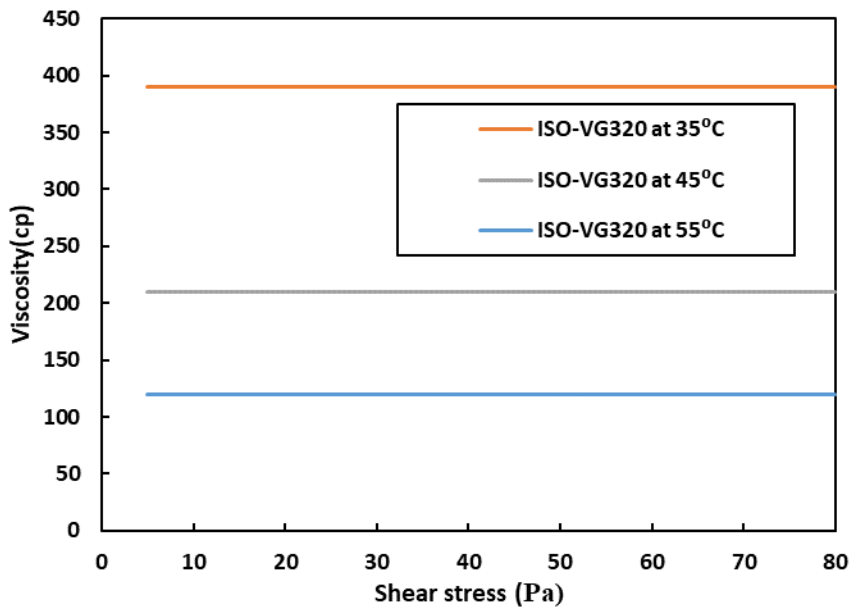

Figure 2.9 ISO-VG320 viscosity versus shear stress

2.2.2 Experimental Procedure

A water test was first performed on the flow loop and then a single-phase oil test. Before testing the ESP, the flow loop was flushed with water to clean the loop. To start water test, tap water was filled from the water tank, then pumping the water by ESP at low rotational speed until the separator was full, the top valve of the separator is open during this time. Then, stop pumping and release some water in the separator to prevent water from getting into the gas line. Afterward the water intake valve and separator top valve were closed to close the flow loop. Use the compressor and pressure regulator to pressurize the separator and maintain the pressure at 50 psig to prevent cavitation problem. Then, the loop was ready for testing water.

To start the oil test, oil is filled from the oil input port on the separator. The PVC pipe in Figure 2.3 indicates the fluid level inside the separator and the liquid level should be higher than the liquid inlet at the right to avoid gas bubble entrainment to the ESP. After injecting part of the oil in the separator while keeping the top valve open, and allowing the flow loop time for oil to move inside the flow loop, oil is added until the liquid level at the PVC pipe reaches the designated level after settling. Next, close the valves and run the ESP at low rotational speed for several minutes to let the separator separate any trapped gas in the loop. Open the valve at the oil input port and see if the oil level has dropped down. Repeat the previous steps and keep adding oil until the liquid level reaches desired level and does not drop again. Then, similar to the water test, close the valves, pressurize the loop and start running the test.

Different rotational speeds of ESP were tested, and different flowrates were set by manipulating the manual valve. Also, different temperature ranges were tested during the single-phase oil experiment. Flow rates, pressure, temperature, and rotational speed data were recorded during the test. Three tests were performed for each flow condition in oil test, and more than 30 data points are used to in calculate the average value to increase accuracy of the measurements. Furthermore, data were collected after ESP ran for 10 minutes to assure stable flow.

2.2.3 Test matrix

The test matrix for water test is listed in Table 2.1 and test matrix for single-phase oil test is listed in Table 2.2.

Table 2.1 Water test matrix

Pump Rotational Speed (rpm)	Manual valve opening (%)
3600, 3000, 2400, 1800	10 to 100

Table 2.2 Single-phase oil test matrix

Pump Rotational Speed (rpm)	Viscosity (cp)	Manual valve opening (%)
3600, 3000	390, 280, 210, 157, 120	20, 30, 40, 50, 60, 70, 80
2400	390, 280, 210, 157	20, 30, 40, 50, 60, 70, 80

2.3 Experimental Results

The results from the data acquisition system include the absolute pressures at ESP inlet and outlet, differential pressures of pump stages, liquid flow rate and liquid temperature. The pressure unit is psi, flow rate is in bpd and temperature is in degree Celsius. In this experiment, pump boosting pressure is converted to the pump head for better comparison between water and oil.

The total pump boosting pressure can be calculated by

$$\Delta Ptotal = Poutlet - Pinlet \tag{2.4}$$

The average pump boosting pressure for each stage is

$$\Delta Pstage = \frac{\Delta Ptotal}{12} \tag{2.5}$$

and the pump head (ft) is

$$H = \frac{\Delta P}{0.433 * \left(\frac{\rho_{liquid}}{\rho_{water}}\right)} \tag{2.6}$$

where ΔP is the differential pump boosting pressure in total or for each stage, and ρ is the density of the liquid in kg/m^3. 1/0.433 is the conversion factor between psi and feet head.

2.3.1 Water performance curve

The MTESP is tested with tap water using four different rotational speeds of 3600 rpm, 3000 rpm, 2400 rpm and 1800 rpm, and the results are shown in Figure 2.10. The pump head (ft) per stage is calculated from total pump boosting pressure (psi) for each flowrate (bpd). The pump curve at 3600 rpm is provided from catalog, and for other rotational speed, the pump curves are obtained by calculation using affinity law. In the figure, experiment data match well with catalog curves, which verifies the testing flow loop.

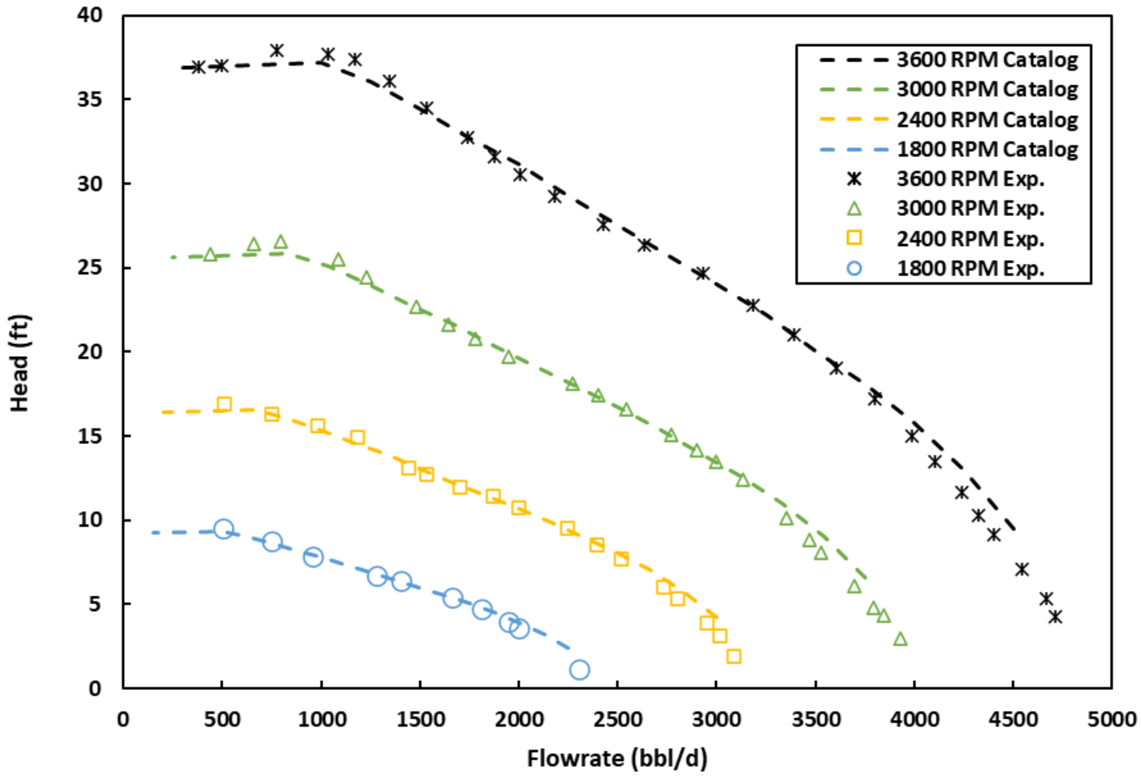

Figure 2.10 MTESP water test performance curve and catalog curve

2.3.2 Single-phase oil performance curve

Lubricating oil ISO-VG320 was used for testing MTESP at three different rotational speeds: 2400 rpm, 3000 rpm, and 3600 rpm. Temperature of the fluid was recorded by the temperature transmitter and the corresponding viscosity of the oil was calculated based on the measurements using rotational viscometer. For 3000 rpm and 3600 rpm rotational speeds, five temperature ranges and viscosities were tested, and for 2400 rpm rotational speed, four viscosities were tested. The pump head versus flowrate curve for rotational speeds 3600 rpm, 3000 rpm and 2400 rpm are shown in Figure 2.11, 2.12 and 2.13. At the same viscosity and same rotational speed, pump head decreases with flow rate increase. Also, pump head decreases with fluid viscosity increase. In addition, pump head at low flow rate range decreases with increase of viscosity.

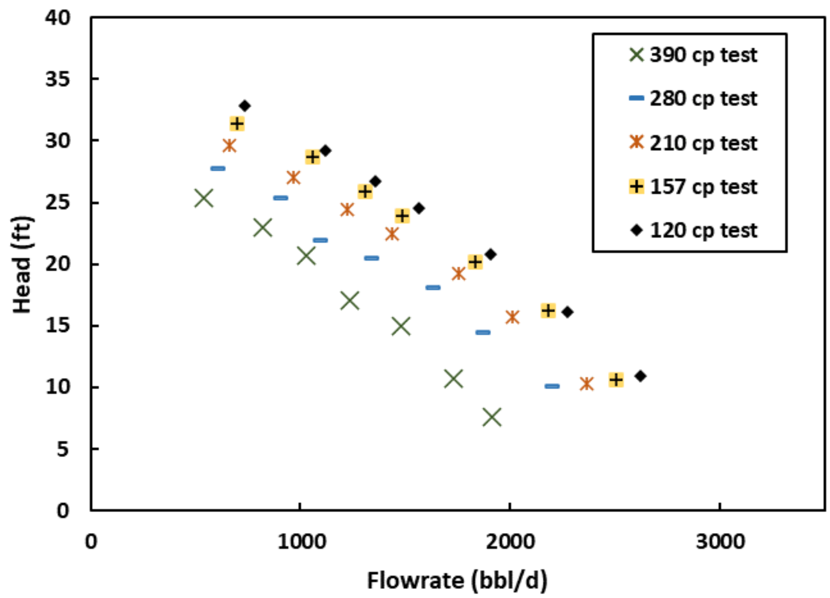

Figure 2.11 MTESP single-phase oil test performance curve at 3600 rpm

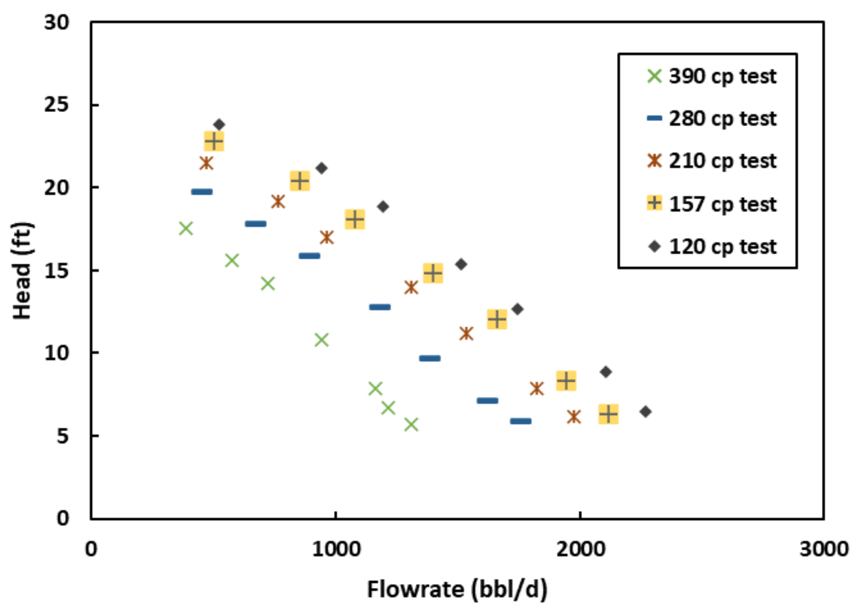

Figure 2.12 MTESP single-phase oil test performance curve at 3000 rpm

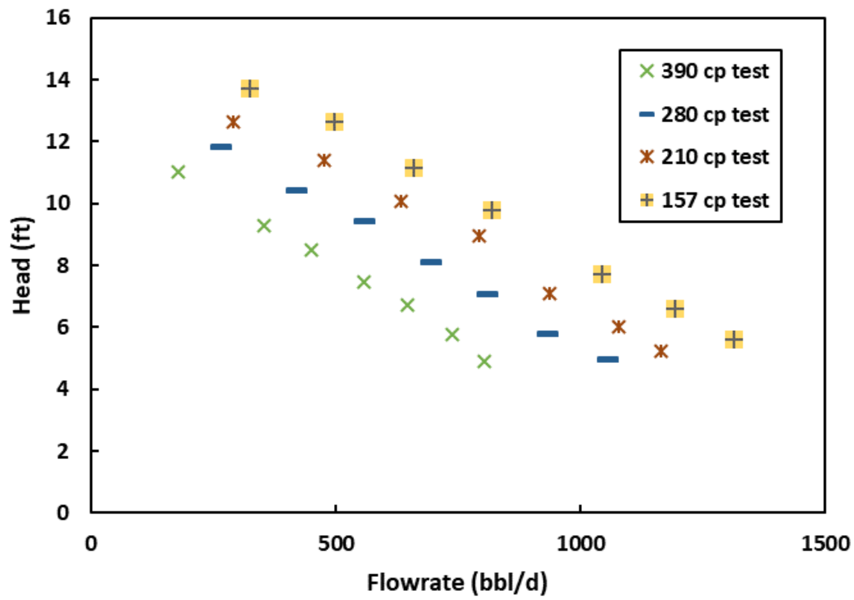

Figure 2.13 MTESP single-phase oil test performance curve at 2400 rpm

CHAPTER 3

THREE-DIMENSIONAL NUMERICAL SIMULATION

This section presents using the three-dimensional numerical simulation to study how liquid viscosity affect the pump head performance. The Computation Fluid Dynamic (CFD) simulations are performed by using commercial software ANSYS Fluent. Pump MTESP and DN1750 are used in simulations. These two pumps were simulated by Zhu (2019) to investigate the ESP erosion effect with water, gas, and sand. In this study, single-phase water and viscous oil flows are simulated for the same ESP geometries, meshes, and simulation setups. The simulation results are presented below.

3.1 ESP Geometry and Mesh

Mesh of two ESP stages is generated for each pump. Figure 3.1 shows the mesh of one stage from MTESP. MTESP is a 4-inch outer diameter mixed type multistage centrifugal pump. For each stage there are 6 blades in the impeller and 8 vanes in the diffuser. The specific speed for this pump is Ns = 2975. The best efficiency point (BEP) of the pump is 3100 bpd flowrate at 3600 rpm rotational speed with the pump head of 24.2 ft. Different grid number of the meshes are tested until the mesh quality reaches the desired level. The single stage mesh grid number in Figure 3.1 is 1.8 million, and the mesh quality value is sufficient for simulation and it is higher than 0.3.

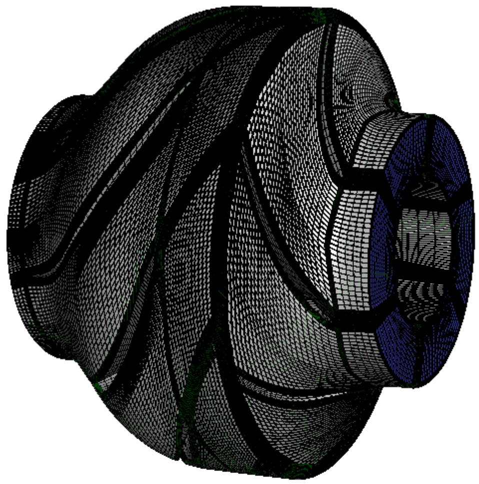

Figure 3.1 Mesh of MTESP

DN1750 is also a 4-inch outer diameter mixed type ESP with BEP equal to 1795 bpd and rotational speed 3500 rpm, and the pump head at this point is 18.7 ft. The specific speed is Ns = 2815. As shown in Figure 3.2, the mesh grid number per stage for DN1750 ESP is 1.2 million.

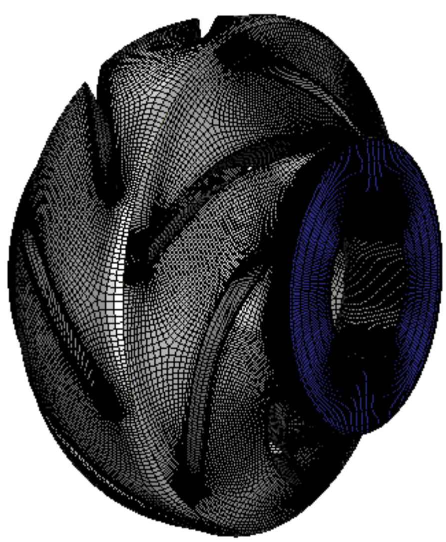

Figure 3.2 Mesh of DN1750

3.2 CFD Simulation Setup and Boundary Conditions

For general setup, steady-state simulation is performed with frozen-rotor technique. Frame motion at impeller zones is applied. In solution methods, coupled scheme is employed for increasing calculation precision.

Two stages of the ESP are used in the simulation and the output parameters at the second stage are recorded. The first stage provides liquid flow pattern at stage outlet that is similar to real pump condition which reduces the stage effect and increases accuracy. The output parameters gathered from the simulation are inlet pressure, outlet pressure, strain, moments, and force at specific conditions to calculate the pressure increment, torque, efficiency, and horsepower for single stage. Testing fluid properties are set with different densities and viscosities. In water test, water density and viscosity are constant with density equal to 1000 kg/m^3 and viscosity 1 cp. For oil test, oil densities are constant based on the experiment oil properties and different oil viscosities are used in simulation. The outlet pressure of the stage diffuser is set to be 70 psig, and the initial gauge pressure is 50 psig which matches separator pressure in the experiment. Three rotational speeds are used in MTESP simulation: 3600 rpm, 3000 rpm, and 2400 rpm. Rotational speed of 3500 rpm is tested for pump DN1750 simulation.

The simulation matrices for the two pumps are listed in Table 3.1 and Table 3.2. A low flow rate of 100 bpd viscous flow is added in the matrices to observe pump performance close to 0 flowrate. Fluid viscosities ranges for experiments are comparable with experimental condition.

Table 3.1 CFD simulation test matrix for MTESP

Viscosity (cp)	1, 10, 25, 50, 100, 120, 157, 200, 210, 280, 300, 390, 500, 1000
Liquid flow rate (bpd)	100, 400, 800, 1200, 1600…

Table 3.2 CFD simulation test matrix for DN1750

Viscosity (cp)	1, 10, 25, 50, 100, 200, 240, 300, 340, 460, 500, 550, 1000
Liquid flow rate (bpd)	100, 400, 800, 1200, 1600…

An example of case input parameters is shown in Table 3.3. Mass flow rate, fluid viscosity and fluid density are the input parameters for each case in CFD simulation. The unit of the inlet flow rate at the impeller inlet is mass flow rate kg/s and it is converted based on volumetric flow rate and fluid density.

Table 3.3 Example of case input parameters and flow rate conversion

Case number	Volumetric flow rate (bpd)	Mass flow rate (kg/s)	Fluid viscosity (cP)	Fluid density (kg/m^3)
1	100	0.184013388	1	1000
2	400	0.736053552	1	1000
3	800	1.472107103	1	1000
4	1200	2.208160655	1	1000
5	100	0.158251514	200	891
6	400	0.633006054	200	891
7	800	1.266012109	200	891
8	1200	1.899018163	200	891
9	100	0.158251514	500	891
10	400	0.633006054	500	891
11	800	1.266012109	500	891
12	1200	1.899018163	500	891

As shown in Figure 3.3, two turbulence model k-ε standard wall function and k-ω shear stress transport (SST) model are tested in water simulation for model selection. There are no large differences from the result comparing these two models. k-ω SST model is used in this study because it can handle the separation at low Reynolds number flow.

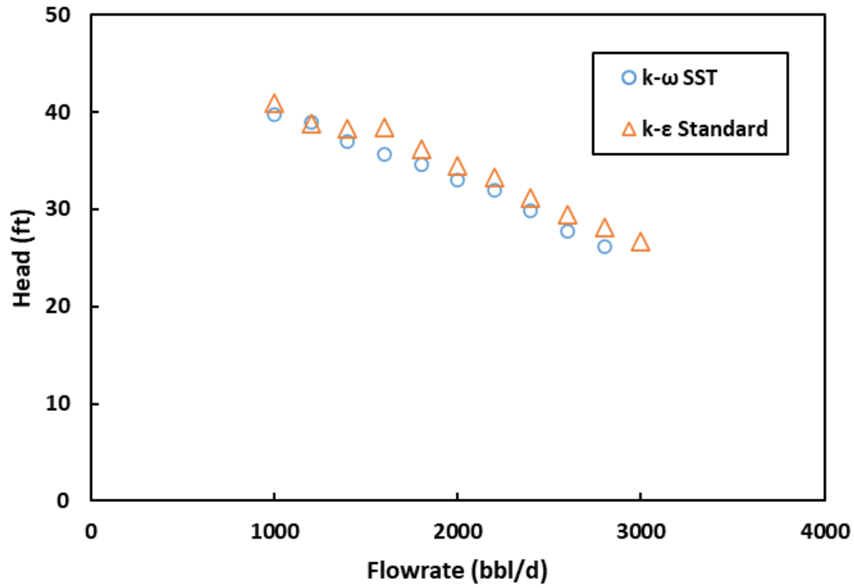

Figure 3.3 Turbulence model selection

The grid number analysis of MTESP is shown in Figure 3.4. When the grid number is higher than 1.5 million, the hydraulic efficiency and pressure increment become stable. As a result, the single stage pump with grid number of 1.8 million is used for MTESP, and the total grid number for two stages is 3.6 million. Same method is also applied on pump DN1750.

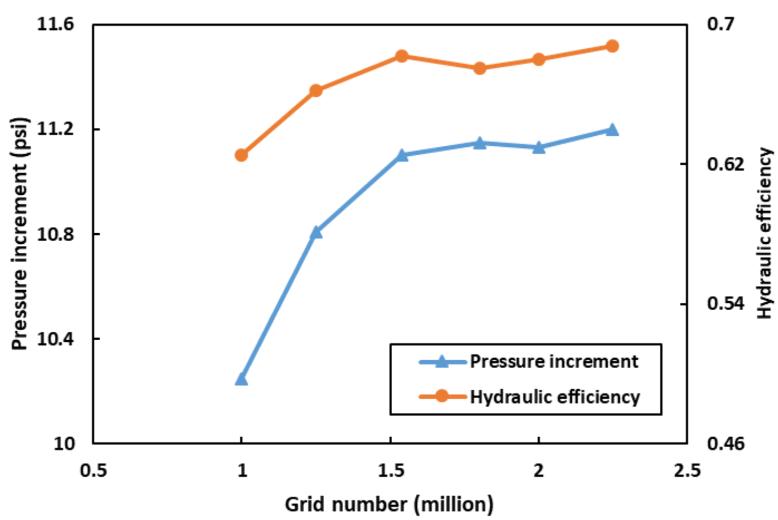

Figure 3.4 Grid number analysis

3.3 Results and Discussions

3.3.1 Simulation validated with water performance

The numerical simulation result for water is compared with experimental data for validation. In Figure 3.5, pump head prediction is compared at 3600 rpm and 3000 rpm, and in Figure 3.6, efficiency comparison is shown for MTESP at 3600 rpm. Overall, the simulation trends agree with experiment curves. However, the simulation predicted performance is about 10% higher than experimental results for both pump head and efficiency. The possible reason is that CFD simulations neglect leakage effect and clearance effect between impeller and diffuser, which means lower pressure and efficiency losses than real operation.

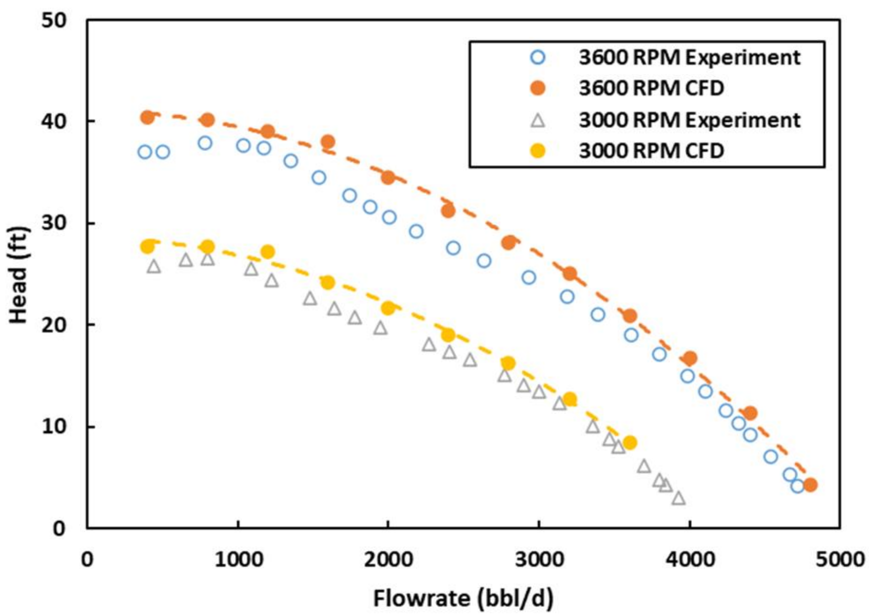

Figure 3.5 MTESP water head validation for CFD simulation

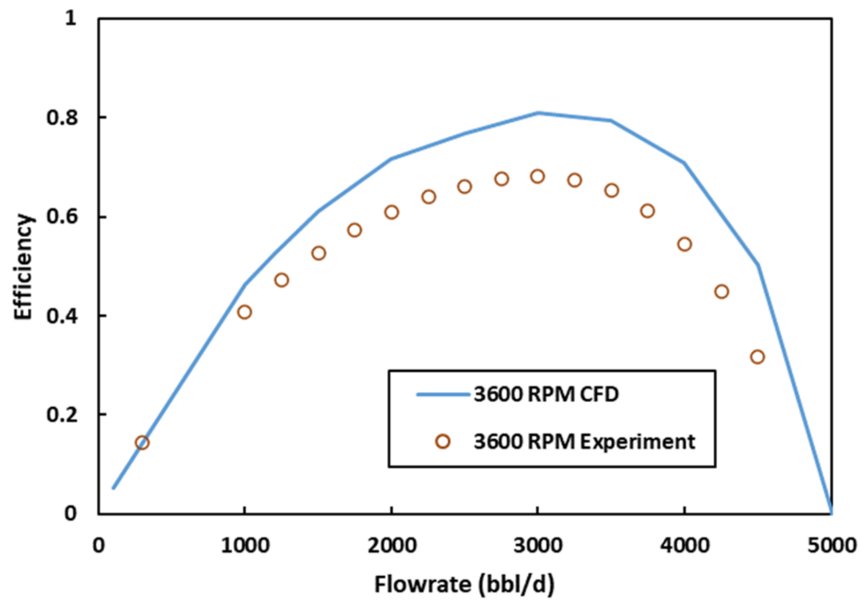

Figure 3.6 MTESP water efficiency validation for CFD simulation

Solano (2009) and Banjar (2013) conducted experiments using DN1750 ESP, their water and single-phase oil experiment data are used in this study. Water head performance at 3500 rpm simulated by CFD is compared with experimental data in Figure 3.7, and the agreement is good.

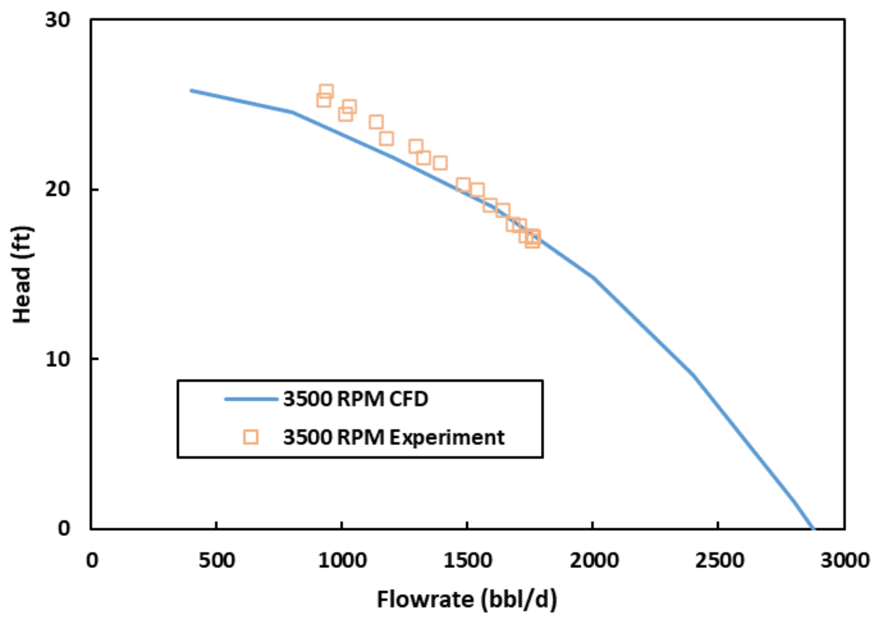

Figure 3.7 DN1750 water head validation for CFD simulation

3.3.2 Simulation compared with oil experiments

Viscous CFD simulation is compared with experimental results for both pumps. Simulations for five viscosities (390, 280, 210, 157, 120 cP) and three rotational speeds (3600, 3000, 2400 rpm) are compared for MTESP in Figure 3.8, 3.9 and 3.10. And the error analysis of MTESP is shown in 3.11. From the results, CFD simulation provides a good prediction in viscous flow, and most of the results are within the 20% error range. The accuracy of the simulation is higher for high rotational speed and low viscosity. In most cases, CFD simulations over predict the experimental data under viscous condition for MTESP.

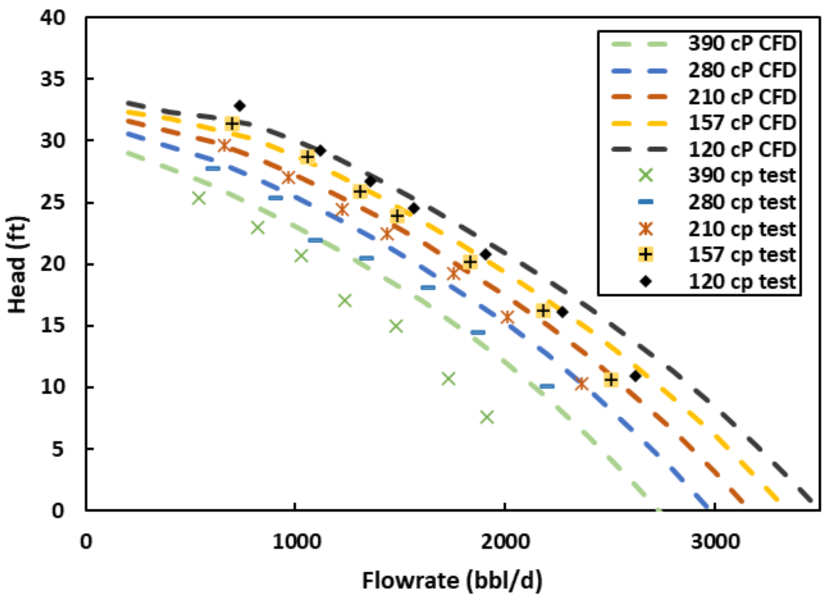

Figure 3.8 Viscous CFD simulation for MTESP at 3600 rpm

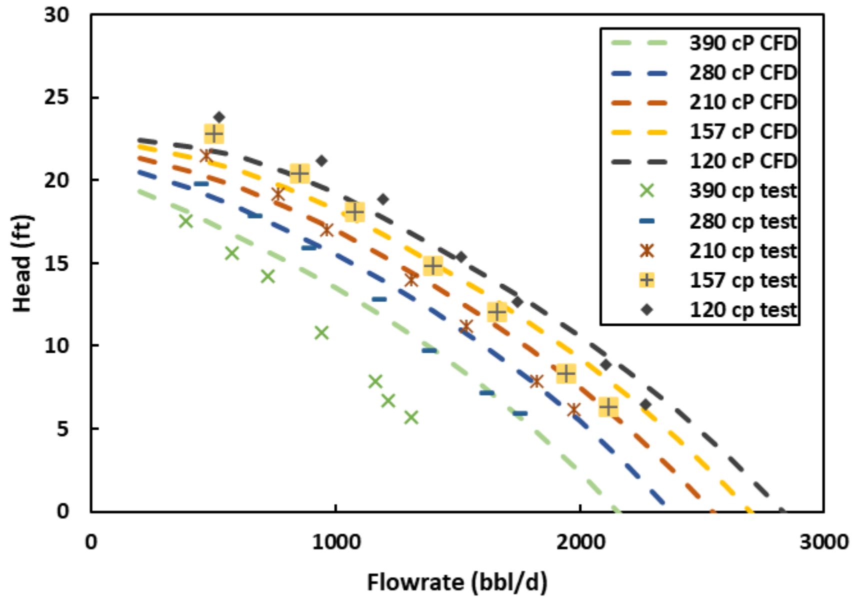

Figure 3.9 Viscous CFD simulation for MTESP at 3000 rpm

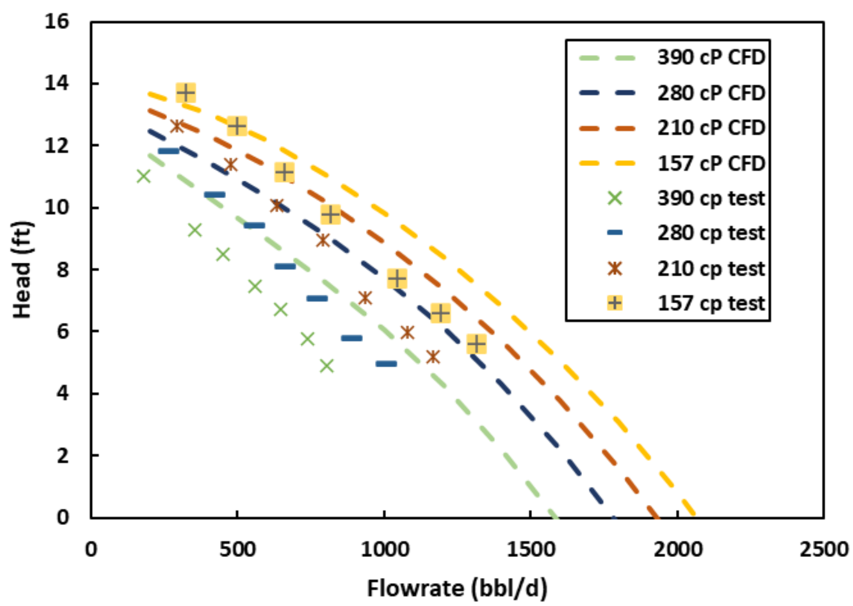

Figure 3.10 Viscous CFD simulation for MTESP at 2400 rpm

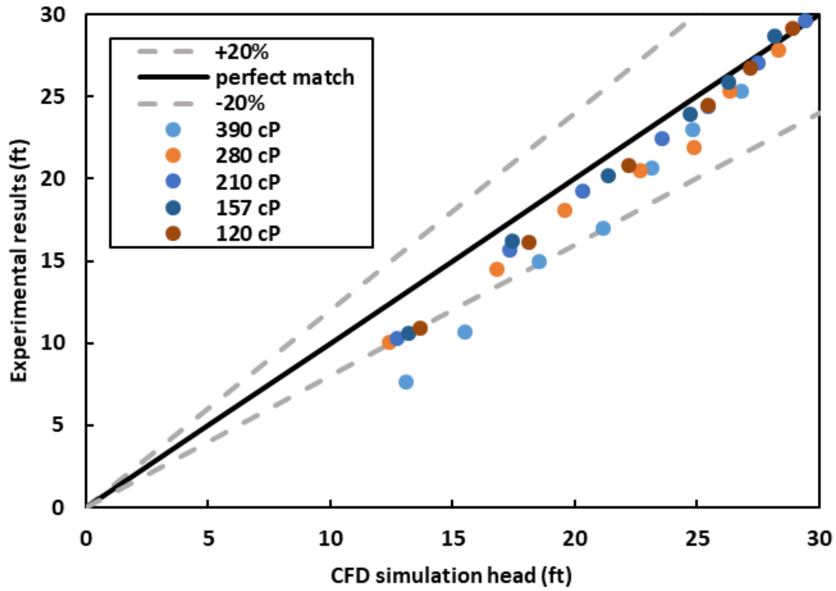

+20%
perfect match
-20%
390 cP
280 cP
210 cP
157 cP
120 cP
Experimental results (ft)
CFD simulation head (ft)
0
5
10
15
20
25
30

(a)

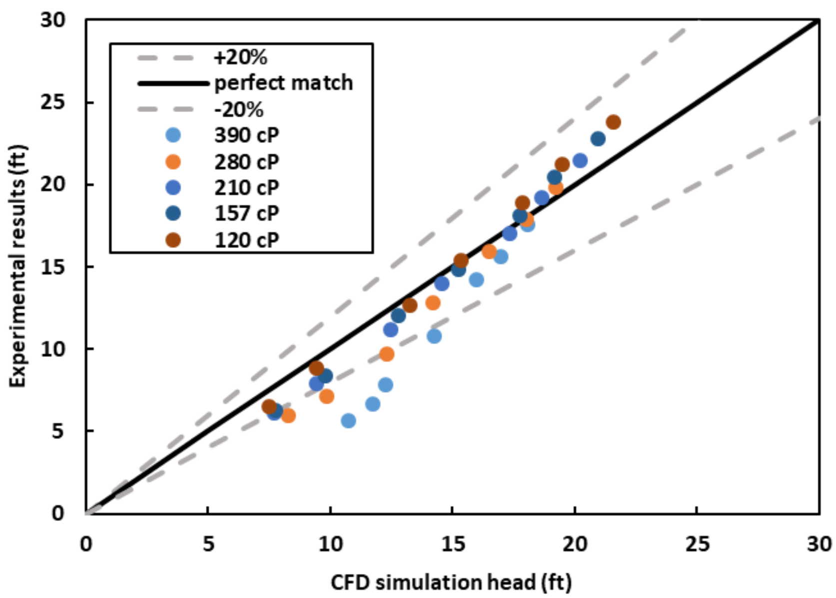

+20%
perfect match
-20%
390 cP
280 cP
210 cP
157 cP
120 cP
Experimental results (ft)
CFD simulation head (ft)
0
5
10
15
20
25
30

(b)

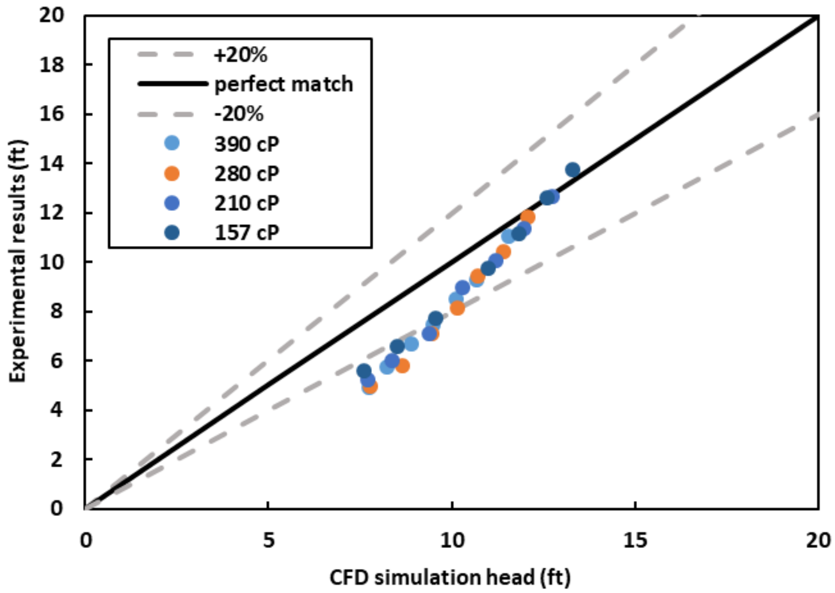

(c)

Figure 3.11 MTESP head comparisons between CFD simulations and experimental results at (a) 3600 rpm (b) 3000 rpm (c) 2400 rpm

Solano (2009) performed single phase oil test for a wide viscosity range. Viscous experimental data at four viscosities (240, 340, 460, 550 cP) are compared with CFD simulations, and the result is shown in Figure 3.12. The results match well with experimental.

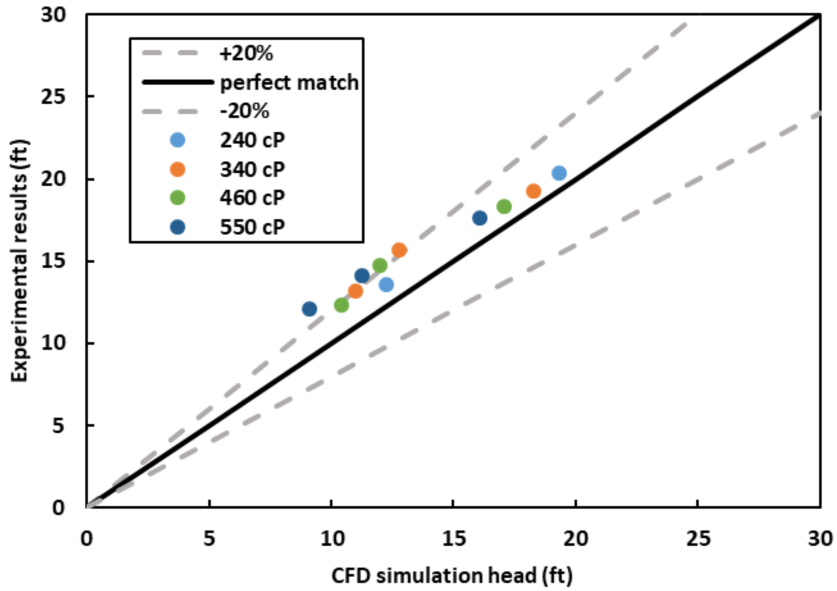

Figure 3.12 DN1750 head comparison between CFD simulations and experiment data under viscous flow

3.3.3 Viscous flow simulation

Figure 3.13 and Figure 3.14 present the single-phase viscous flow CFD simulation results of pump head for MTESP at 3600 rpm and DN1750 at 3500 rpm. The viscosity range is from water to 1000 cP fluids. In both pumps, it can be observed that pump heads decrease with the increases of fluid viscosity at constant flowrate. And, when the fluid viscosity reaches 1000 cP, the pump head decline curve becomes linear due to flow regime change from turbulent to laminar.

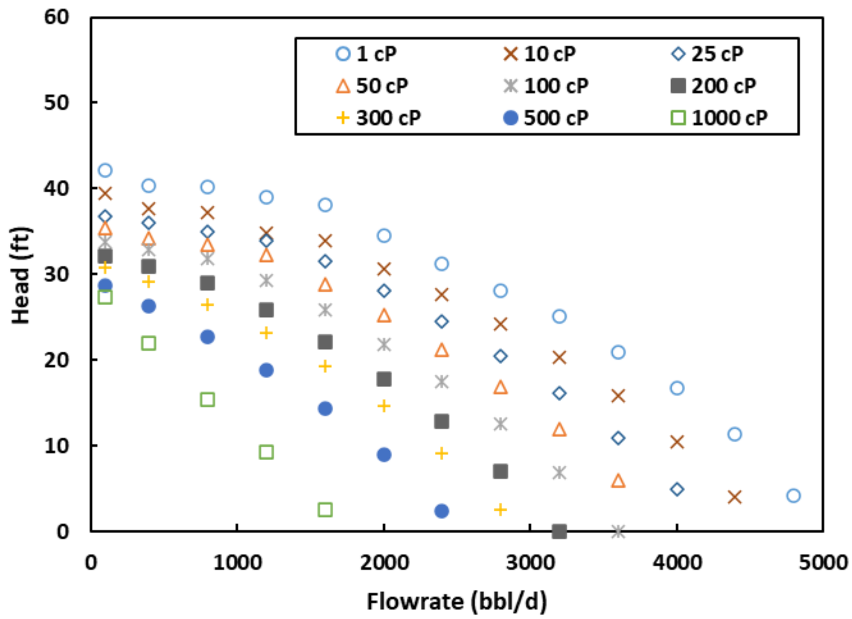

Figure 3.13 Single-phase viscous flow CFD simulation results for MTESP at 3600 rpm

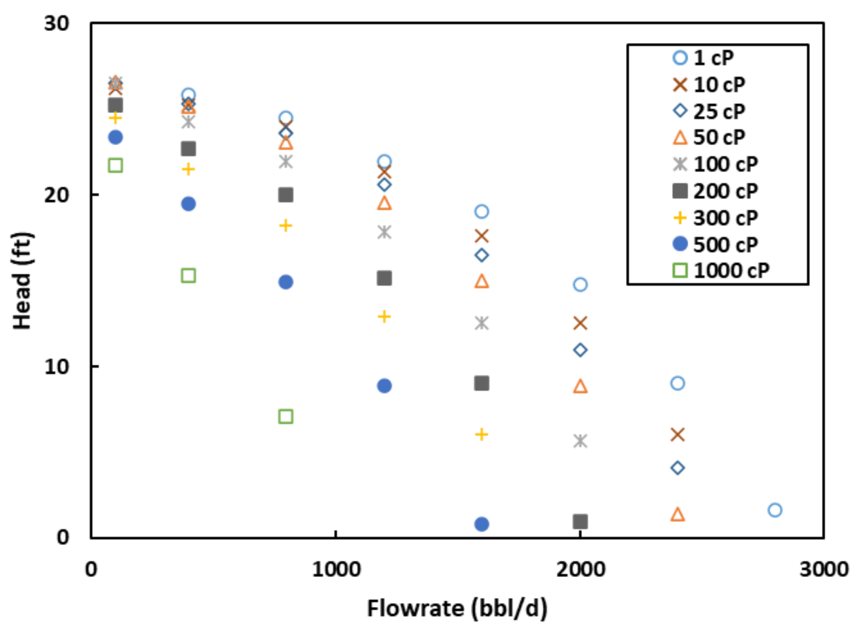

Figure 3.14 Single-phase viscous flow CFD simulation results for DN1750 at 3500 rpm

Comparing the CFD simulation results, the influence of fluid viscosity on pump performance is different for these two pumps. Compared to pump DN1750, the head deviation from water to 100 cP fluid is higher in Figure 3.13. Similar behavior can also be found in Amaral's study (2009), where a big head reduction from 1 to 60 cP is found in both radial pump and semi-axial pump. The reason for this phenomenon is presumably due to different pump characteristics.

Although the pump head at zero flow rate is believed to stay the same when fluid viscosity changes, the simulated head curves of both ESPs shift down due to the increase of fluid viscosity. At the low flow rate region, the simulated and tested pump head of DN1750 decreases around 10% from 10 cP to 500 cP, while that of MTESP decreases around 30%. Similar behavior can also be found in Barrios et al. (2012) for the mixed-type WJE 1000 pump. In addition, the experiments conducted by Ippen (1946) show a 5% degradation of the pump head from 1 cP to 460 cP for a pump with Ns = 2622. But for the pump with Ns = 1163, head curves converged at the low flow rate from 1 cP to 2020 cP. In section 4.3 of this study, the head of TE2700, Ns = 1600, also stays the say at zero flow rate condition. Therefore, it is presumed that the boosting pressure at zero flow rate conditions tends to decrease from radial type ESP to mixed type ESP when the pump specific speed increases and the pump tends to become closer to an axial type pump. As a summary, the trend of pump head performance degradation under viscous flow conditions is affected by pump characteristics. For mixed-type pumps, the head reduction can be observed at zero flow rate when viscosity increases. Since the ideal Euler head assumes the fluid radial velocity is the same to the shaft rotating velocity, several studies (Wiesner 1967; Thin et al. 2008; Bing et al. 2012, Zhu et al. 2019, 2020, and 2021) have introduced a slip factor to describe the mismatch between the ideal and the real velocity at the impeller outlet. According to the CFD and test results in this study, it is presumable that the slip factor is affected by the fluid viscosity. In addition, even no fluid flows through the pump, the velocity still fluctuates in pump stages. It can be considered in the mechanistic model prediction that the slip factor is more obviously affected for mixed-type pumps

CHAPTER 4

MECHANISTIC MODELING AND RESULTS

This chapter discusses the modification of previous mechanistic model of ESP performance prediction for single-phase flow conditions (Zhu et al., 2019). The model modification is based on the head reduction effect for mixed-type pump and turn loss for viscous flow. The comparisons of modified mechanistic model predictions with experimental data are presented.

4.1 Mechanistic Modeling of ESP Single-Phase Liquid Performance

Based on the Euler's equation for centrifugal pump, the mechanistic model predicts the ESP boosting pressure by considering losses due to viscosity effect. The losses include recirculation, turning, friction and leakage losses. The pump performance is the Euler head minus losses.

4.1.1 Euler's equation

Euler's equation is based on assumptions of no losses, steady state flow, and incompressible fluid (Vieira et al. 2015). Figure 4.1 shows the velocity triangles at impeller inlet and outlet.

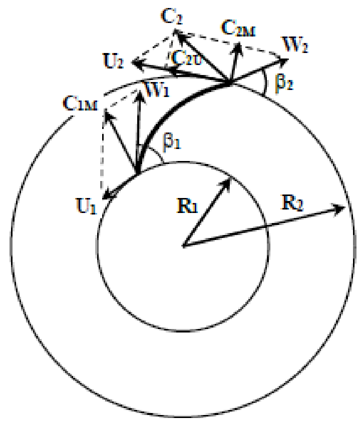

Figure 4.1 Velocity triangles at impeller inlet and outlet

From Figure 4.1, the inner circle represents the impeller inlet, and the outer circle is the impeller outlet. *R* is impeller radius, *U* is the impeller tangential velocity, *β* is the blade angle from tangential, *W* is relative velocity, *C* is the absolute fluid velocity, C_M is the meridional velocity, and C_U is the fluid tangential velocity. Subscript 1 means the term is acting on impeller inlet, and 2 means acting on impeller outlet. The Euler's theoretical head for pump performance prediction is:

$$H_E = \frac{U_2 C_{2U} - U_1 C_{1U}}{g} \tag{4.1}$$

where H_E is the Euler head, *g* is gravitational acceleration. The Euler's equation can be rewritten based on the velocity components as:

$$H_E = \frac{U_2^2 - U_1^2}{2g} + \frac{W_1^2 - W_2^2}{2g} + \frac{C_2^2 - C_1^2}{2g} \tag{4.2}$$

The tangential velocity at impeller inlet and outlet is:

$$U_1 = R_1 \Omega \tag{4.3}$$

$$U_2 = R_2 \Omega \tag{4.4}$$

where *Ω* is angular velocity which can be calculated by rotational speed *N* in rpm:

$$\Omega = \frac{2\pi N}{60} \tag{4.5}$$

The meridional velocity at impeller inlet and outlet are:

$$C_{1M} = \frac{Q + Q_{LK}}{(2\pi R_1 - Z_I T_B) y_{I1}} \tag{4.6}$$

$$C_{2M} = \frac{Q + Q_{LK}}{(2\pi R_2 - Z_I T_B) y_{I2}} \tag{4.7}$$

where Q and Q_{LK} are liquid flow rate and leakage flow rate, Z_I is the impeller blade number, T_B is the blade thickness projected to the radial direction, and y_I is the impeller inlet height at inlet and outlet location. The relative velocities at impeller inlet and outlet are:

$$W_1 = \frac{C_{1M}}{\sin \beta_1} \tag{4.8}$$

$$W_2 = \frac{C_{2M}}{\sin \beta_2} \tag{4.9}$$

The absolute fluid velocity at the impeller inlet and outlet are:

$$C_1 = \sqrt{C_{1M}^2 + \left(U_1 - \frac{C_{1M}}{\tan \beta_1}\right)^2} \tag{4.10}$$

$$C_2 = \sqrt{C_{2M}^2 + \left(U_2 - \frac{C_{2M}}{\tan \beta_2}\right)^2} \tag{4.11}$$

The fluid tangential velocity at impeller inlet and outlet are:

$$C_{1U} = U_1 - W_1 \cos \beta_1 \tag{4.12}$$

$$C_{2U} = U_2 - W_2 \cos\beta_2 \tag{4.13}$$

Substituting equations into Eq. (4.1), the Euler equation can be rewritten as:

$$H_E = \frac{U_2(U_2 - W_2 \cos \beta_2) - U_1(U_1 - W_1 \cos \beta_1)}{g} \tag{4.14}$$

If no fluid rotation at the impeller inlet, the equation can be rewritten as:

$$H_E = \frac{U_2^2}{g} - \frac{U_2 C_{2M}}{\mathrm{gtan}\,\beta_2} \tag{4.15}$$

Slip coefficient σ_s is used for Euler's head correction based on Wiesner (1967):

$$\sigma_s = 1 - \frac{\sqrt{\sin\beta_2}}{Z_I^{0.7}} \tag{4.16}$$

In this study, a modified slip coefficient is used to account for head reduction behavior by mixed-type ESP under viscous condition. In the equation, pump specific speed *Ns* is used for identification of the pump type within the range of 1000 to 2975. μ is the liquid viscosity and μ_w is the water viscosity. The slip coefficient is modified as:

$$\sigma_s = 1 - \frac{\sqrt{\sin\beta_2}}{Z_I^{1.6}} \times \frac{\mu}{\mu w \times 175}^{\left(\frac{Ns}{2975}\right)^4} \tag{4.17}$$

The Euler head can be rewritten as:

$$H_E = \sigma_s \frac{U_2^2}{g} - \frac{U_2 C_{2M}}{\mathrm{gtan}\,\beta_2} \tag{4.18}$$

4.1.2 Head losses

The term of best match flow rate (Q_{BM}) is introduced in the model which corresponds to the flow direction at the impeller outlet matching the designed flow direction. Recirculation losses occur when there is a mismatch of the flow direction at flow rate different from Q_{BM}. Figure 4.2 is the scenario of flow rate less than Q_{BM}.

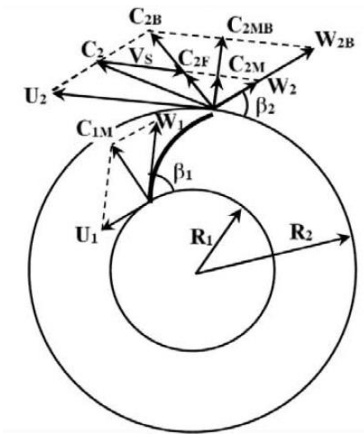

Figure 4.2 Velocity triangles at impeller outlet

where C_{2B} is the absolute fluid velocity at the impeller outlet at Q_{BM}, C_{2MB} is the meridional velocity at the impeller outlet corresponding to Q_{BM}, W_{2B} is the fluid relative outlet velocity corresponding to Q_{BM}, C_{2F} is the fluid flow velocity at Q_{BM} direction, and Vs is the shear velocity.

The flow rate at best match point is affect by fluid viscosity and rotational speed, the new Q_{BM} is:

$$Q_{BM} = Q_{BM,water} \frac{N}{N_{ref}} \left(\frac{\mu}{\mu_w}\right)^{0.16*\left(\frac{34.48}{N_S}\right)^4} \tag{4.19}$$

Current flow rate accounts leakage flow which is $Q+Q_{LK}$. When $Q+Q_{LK} < Q_{BM}$, the fluid flow velocity outside the impeller is:

$$C_{2F} = C_{2B} \frac{Q + Q_{LK}}{Q_{BM}} \tag{4.20}$$

The shear velocity is:

$$V_S = U_2 \frac{Q_{BM} - (Q + Q_{LK})}{Q_{BM}} \tag{4.21}$$

The C_{2P} is the projected velocity of C_2 in the direction of C_{2B}, it is in the direction of Q_{BM}, which can be obtain from:

$$C_2^2 - C_{2P}^2 = V_S^2 - (C_{2P} - C_{2F})^2 \tag{4.22}$$

Solving the equation:

$$C_{2P} = \frac{C_2^2 + C_{2F}^2 - V_S^2}{2C_{2F}} \tag{4.23}$$

Only partial kinetic energy is converted to static pressure due to the shear effect of fluid recirculation in impeller. The recirculation is dependent on the shear velocity, the channel size, and the fluid viscosity. A Reynolds number is used to estimate the recirculation effect:

$$Re_C = \frac{\rho V_S D_C}{\mu} \tag{4.24}$$

where D_C is the representative impeller channel width:

$$D_C = \frac{2\pi R_2}{Z_I} \sin\beta_2 - T_B \tag{4.25}$$

A shear factor due to viscosity can be described as:

$$\sigma = \frac{\left(\frac{\mu_w}{\mu}\right)^{0.1}}{10 + 0.02Re_c^{0.25}} \tag{4.26}$$

A correlation of effective velocity is:

$$C_{2E} = C_{2F} + \sigma(C_{2P} - C_{2F}) \tag{4.27}$$

When Q+Q_{LK} > Q_{BM}, the V_S equations changes to:

$$V_S = U_2 \frac{(Q + Q_{LK}) - Q_{BM}}{Q_{BM}} \tag{4.28}$$

C_{2E} can be expressed as:

$$C_{2E} = \frac{C_2^2 + C_{2F}^2 - V_S^2}{2C_{2F}} \tag{4.29}$$

The recirculation loss H_R can be calculated by:

$$H_R = \frac{C_2^2 - C_{2E}^2}{2g} \tag{4.30}$$

The effective Euler head H_{EE} for both Q+Q_{LK} < Q_{BM} and Q+Q_{LK} > Q_{BM} is:

$$H_{EE} = H_E + \frac{C_{2E}^2 - C_2^2}{2g} \tag{4.31}$$

The friction loss in the impeller and diffuser can be treated as channel flow and can be expressed using channel flow friction loss equation:

$$H_{FI} = f_{FI} \frac{V_I^2 L_I}{2gD_I} \tag{4.32}$$

and

$$H_{FD} = f_{FD} \frac{V_D^2 L_D}{2gD_D} \tag{4.33}$$

where the subscript *I* and *D* represent the impeller and diffuser, H_F is the friction loss, f_F is the friction factor, *V* is the representative fluid velocity, *L* is the channel length, and *D* is the representative (hydraulic) diameter of the channel. The friction factor is calculated from the Sun and Prado (2006) correlation which includes Churchill (1977) friction factor. Channel shape effect, blade curve effect, and pump rotational speed effect (F_γ, F_β, and F_ω) are accounted in friction factor calculation:

$$f_F = F_\gamma F_\beta F_\omega f \tag{4.34}$$

where *f* is the Churchill friction factor and F_γ, F_β, and F_ω can be calculated from Sun and Prado (2006).

$$f = 8\left[\left(\frac{8}{Re}\right)^{12} + \frac{1}{(A+B)^{1.5}}\right]^{\frac{1}{12}} \tag{4.35}$$

A and *B* can be expressed as:

$$A = \left[2.457 \ln\left(\frac{1}{\left(\frac{7}{\mathrm{Re}}\right)^{0.9} + 0.27\frac{\varepsilon}{D}}\right)\right]^{16} \tag{4.36}$$

$$B = \left(\frac{37530}{\text{Re}}\right)^{16} \quad (4.37)$$

where the ε is the pipe roughness, and Reynolds numbers in the impeller and diffuser are:

$$\text{Re}_I = \frac{\rho V_I D_I}{\mu} \quad (4.38)$$

$$\text{Re}_D = \frac{\rho V_D D_D}{\mu} \quad (4.39)$$

The representative diameters of impeller and diffuser channels are given by:

$$D_I = \frac{4\text{Vol}_I}{A_{SI}} \quad (4.40)$$

and

$$D_D = \frac{4\text{Vol}_D}{A_{SD}} \quad (4.41)$$

where *Vol* is the volume of the channel and A_S is the total wall area of the channel. The representative fluid velocity in impeller and diffuser channel are given by:

$$V_I = \frac{Q + Q_{LK}}{A_I Z_I} \quad (4.42)$$

and

$$V_D = \frac{Q}{A_D Z_D} \quad (4.43)$$

where *A* is the representative impeller or diffuser channel cross sectional area and *Z* is the blade and vane number for impeller and diffuser. A_I and A_D can be defined as:

$$A_I = \frac{Vol_I}{L_I} \quad (4.44)$$

and

$$A_D = \frac{Vol_D}{L_D} \quad (4.45)$$

The turning loss occurs when the fluid flow direction changes in the impeller and diffuser, the head losses due to turning loss H_T can be estimated as:

$$H_T = f_T \frac{V^2}{2g} \tag{4.46}$$

where f_T is turning loss factor which is determined from experiments. The modified turning loss equation can be rewritten including the viscous effect as

$$H_{TI} = f_{TI} \frac{V_I^2}{2g} \left(\frac{\mu}{\mu w}\right)^{0.1} \tag{4.47}$$

and

$$H_{TD} = f_{TD} \frac{V_D^2}{2g} \left(\frac{\mu}{\mu w}\right)^{0.1} \tag{4.48}$$

where the subscripts *I* and *D* represent impeller and diffuser. The modified equation indicates that the turning loss increases as the fluid viscosity increases.

The leakage flow occurs when fluid flow through clearance and balance holes, the leakage loss H_{LK} can be calculated by:

$$H_{LK} = H_{IO} - \frac{U_2^2 - U_{LK}^2}{8g} \tag{4.49}$$

where H_{IO} is the head increase across the impeller and U_{LK} is the tangential velocity due to the impeller rotation at the leakage, which can be calculated by:

$$U_{LK} = R_{LK}\Omega \tag{4.50}$$

where R_{LK} is the radius of the leakage clearance. The head increase across the impeller can be described as:

$$H_{IO} = H_{EE} - H_{FI} - H_{TI} \tag{4.51}$$

Contraction, expansion, and friction components are considered in head loss due to leakage, which is calculate by:

$$H_{LK} = 0.5\frac{V_L^2}{2g} + 1.0\frac{V_L^2}{2g} + f_{LK}\frac{V_L^2 L_G}{2gS_L} \tag{4.52}$$

where L_G is the leakage channel length, S_L is the width of the leakage, f_{LK} is the friction loss coefficient in leakage regions. The fluid velocity through the leakage V_L can be described as:

$$V_L = \sqrt{\frac{2gH_{LK}}{f_{LK}\frac{L_G}{S_L} + 1.5}} \tag{4.53}$$

Assuming the friction factor f_{LK} can be estimated based on Churchill (1977) equations, the Reynolds number can be calculated as:

$$\mathrm{Re}_L = \frac{\rho V_L S_L}{\mu} \tag{4.54}$$

And the leakage flow rate is:

$$Q_{LK} = 2\pi R_{LK} S_L V_L \tag{4.55}$$

4.2 Mechanistic Model Setup

In this study, experimental results for three different ESP are used to compare with the mechanistic model. Banjar (2018) conducted experiments using mixed-type ESP DN1750, Zhang (2017) conducted experiments using radial type ESP TE2700, and mixed-type ESP MTESP are included in the experimental results comparison.

The summary of pump characteristics is provided in Table 4.

Table 4.1 The summary of pump characteristics

Pump Name	*Ns* (-)	Z_I (-)	Z_D (-)	Q_{BEP} (bpd)
MTESP	2975	6	8	3100
DN1750	2815	6	8	1795
TE-2700	1600	5	9	2750

To find the best match flow rate, the mechanistic model is adjusted to match catalog curve for all three pumps. As shown in Figure 4.3, the best match flow rate Q_{BM} for MTESP is 7500 bpd, for pump DN1750 is 4000 bpd, and for pump TE2700 is 7000 bpd. The model curves match well with catalog curves.

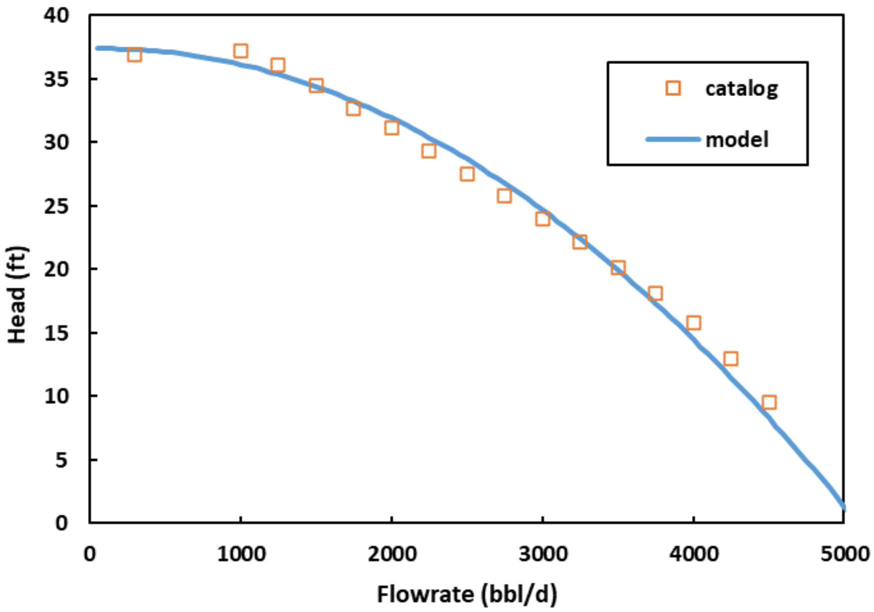

(a)

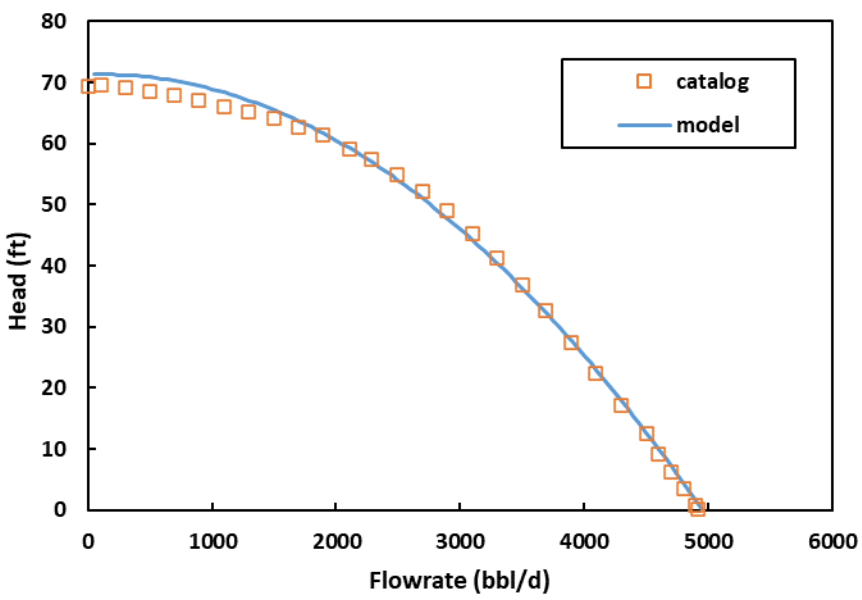

(b)

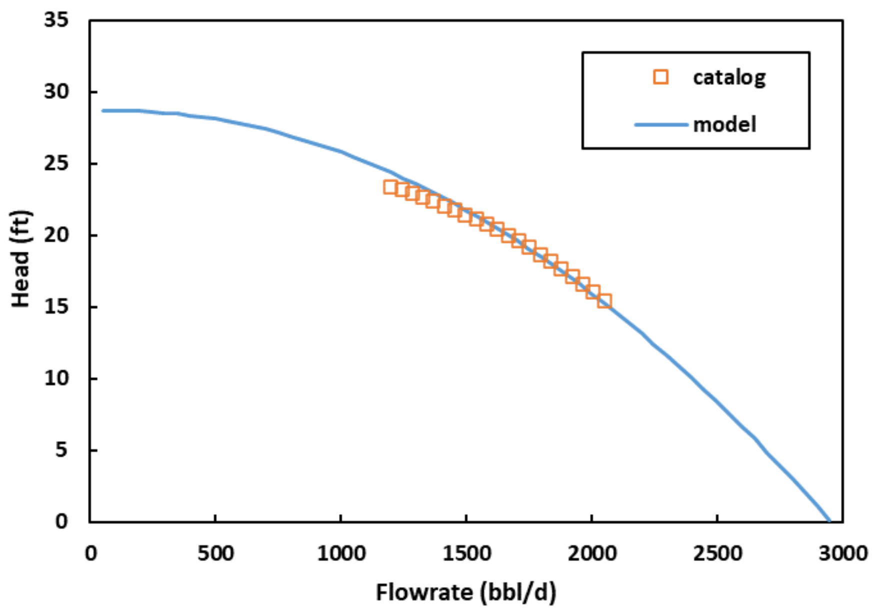

(c)

Figure 4.3 Model matches with catalog data for ESP (a) MTESP (b) TE2700 (c) DN1750

4.3 Mechanistic Modeling Validation

4.3.1 MTESP validation

Water and single-phase oil performance data at 3600, 3000 and 2400 rpm rotational speeds are compared with the mechanistic model predictions. Figure 4.4 shows the measured water heads and the corresponding model predicted heads, with good agreement.

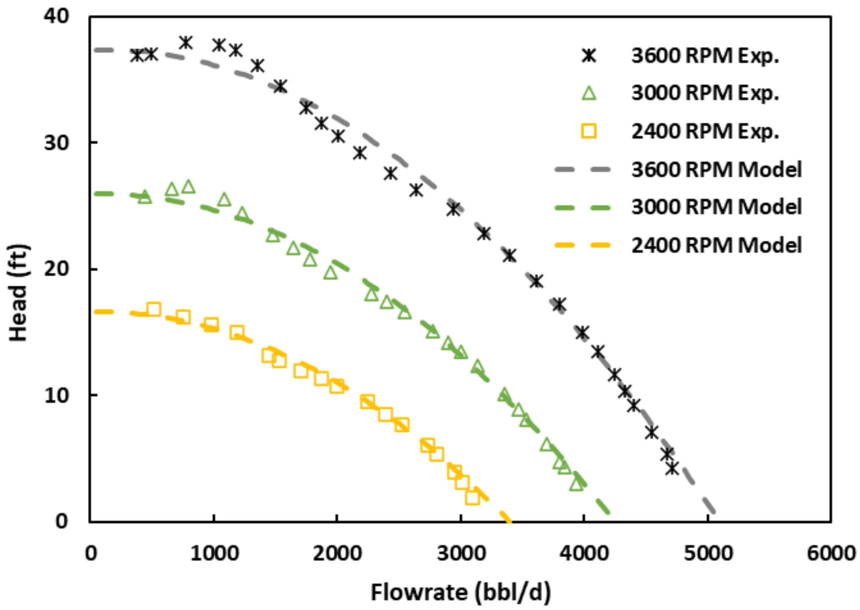

Figure 4.4 MTESP water performance model validation

Figures 4.5, 4.6, and 4.7 present the model predictions compare with the measured ESP head performance under viscous conditions at 3600, 3000, and 2400 rpm. Viscosities 390, 280, 210, 157, and 120 cP are used in the validation. The model predictions agree with experimental data. Figure 4.8 shows that most of the data is in 20% range of error in comparison. The model accounts for mixed-type pump behavior under viscous flow and the head shifts down due to high viscosity.

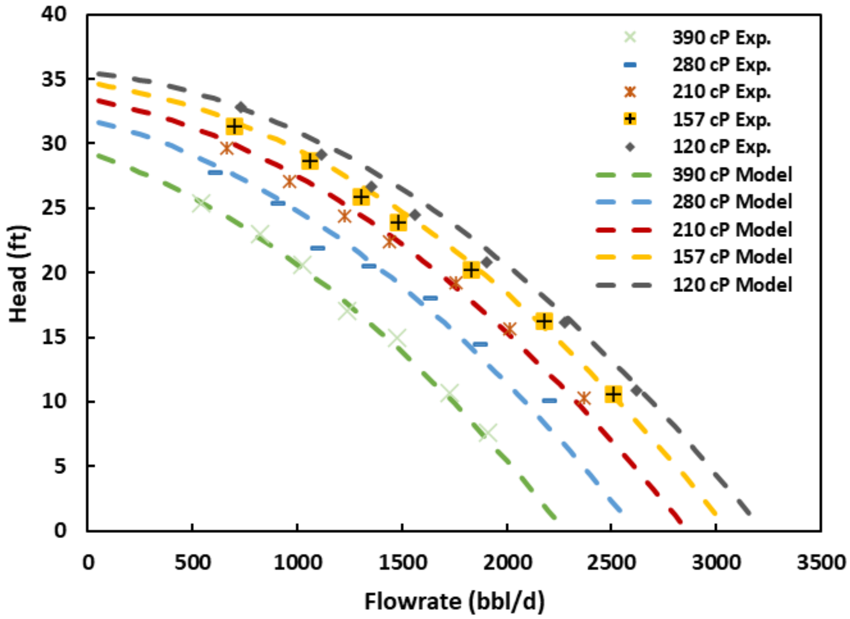

Figure 4.5 MTESP viscous performance model validation at 3600 rpm

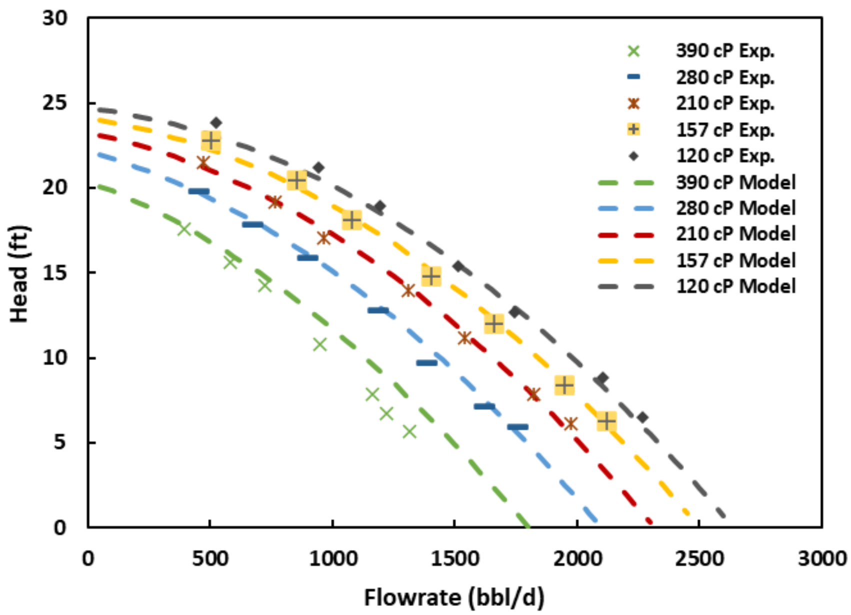

Figure 4.6 MTESP viscous performance model validation at 3000 rpm

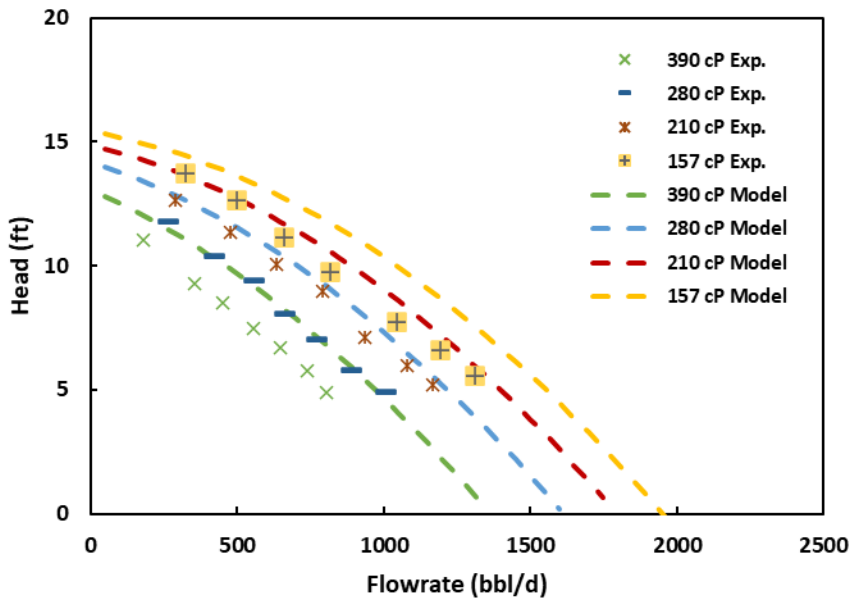

Figure 4.7 MTESP viscous performance model validation at 2400 rpm

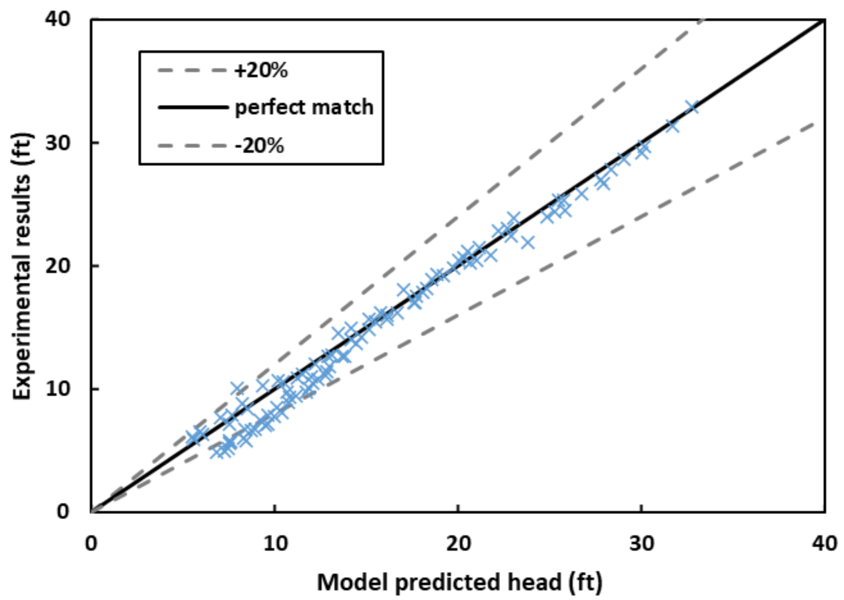

Figure 4.8 Differences between model predicted heads and experimental results for MTESP

4.3.2 DN1750 Validation

Water and single-phase oil experiment performance data conducted by Banjar (2018) at 3500 rpm rotational speed is compared with the modified mechanistic model of this study. Figure 4.9 shows the measured water head, catalog curve and model predicted head. The model prediction is higher than experiment but matches the catalog, this is because the pump was in worn out condition.

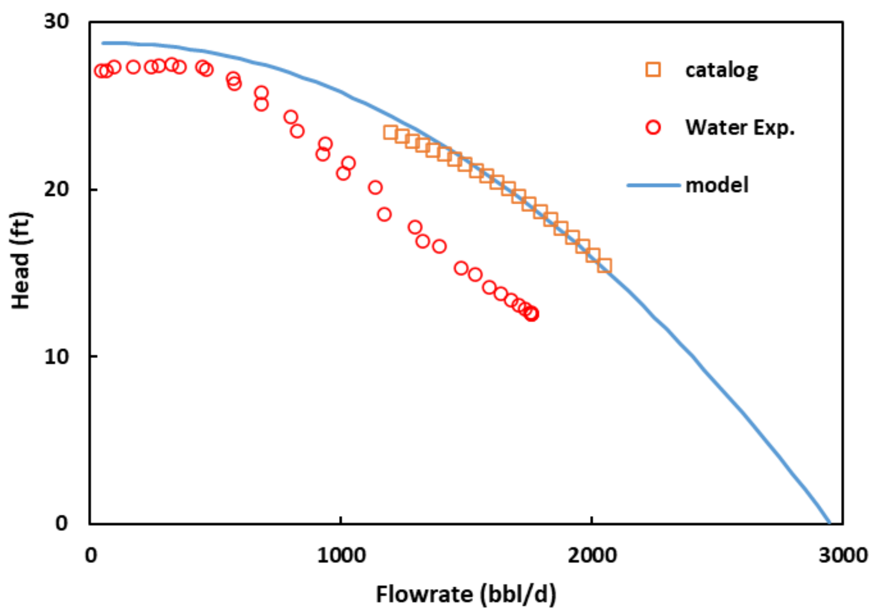

Figure 4.9 DN1750 water performance model validation

Figure 4.10 and Figure 4.11 shows the comparison between model and viscous flow experiments. Despite the pump degradation due to worn out condition, the trend of the model prediction matches experimental results. The head reduction due to viscous effect for mixed-type ESP can be found in both model and experiment data.

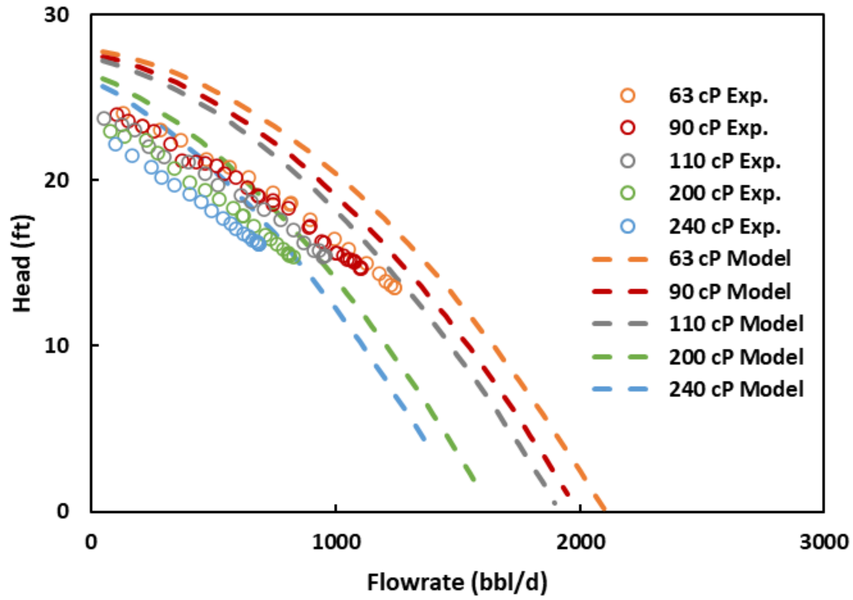

Figure 4.10 DN1750 viscous performance model validation at 3500 rpm

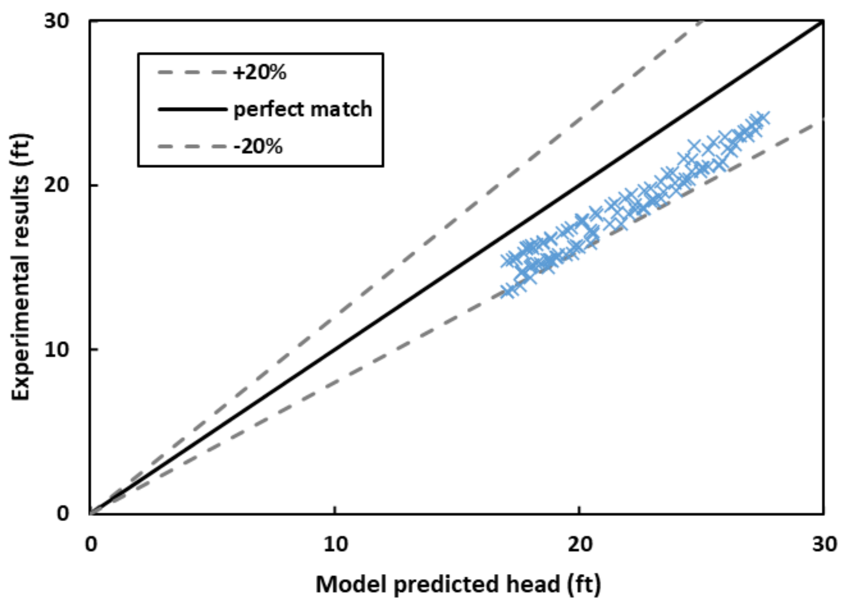

Figure 4.11 Differences between model predicted heads and experimental results for DN1750

4.3.3 TE2700 validations

TE2700 viscous flow performance from experiments is compared with model at 3500 and 2400 rpm as shown in Figures 4.12 and 4.13. The differences are shown in Figure 4.14. The head curves from model agrees with the experimental results and the mixed-type pump behavior does not show on the radial-type pump.

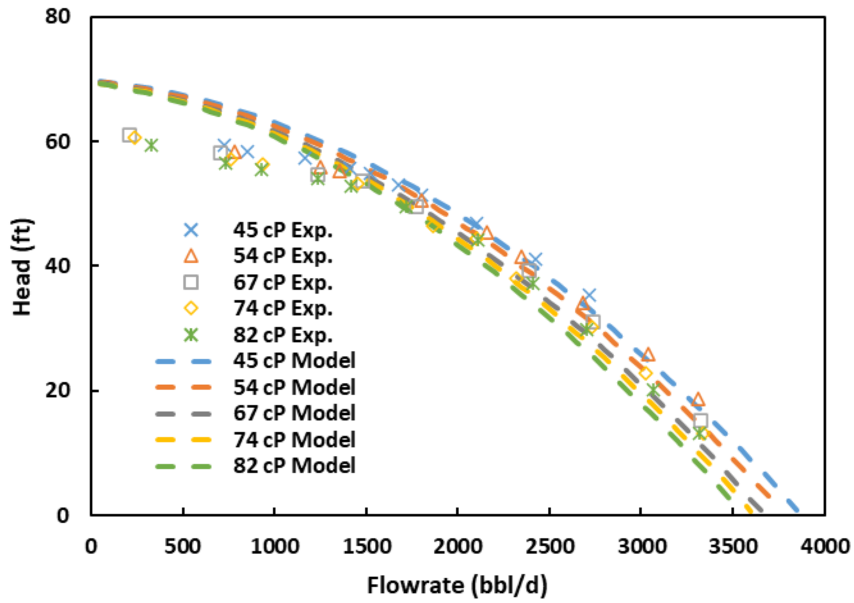

Figure 4.12 TE2700 viscous performance model validation at 3500 rpm

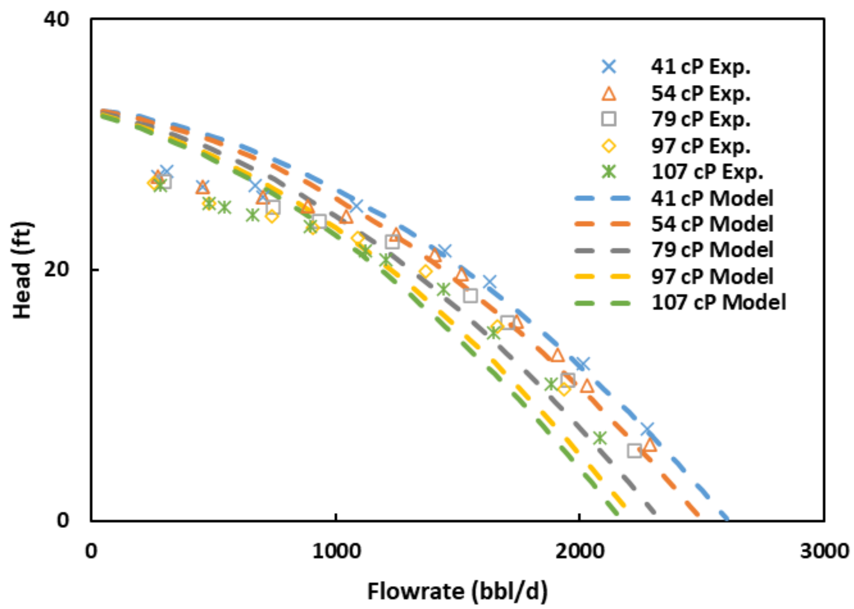

Figure 4.13 TE2700 viscous performance model validation at 2400 rpm

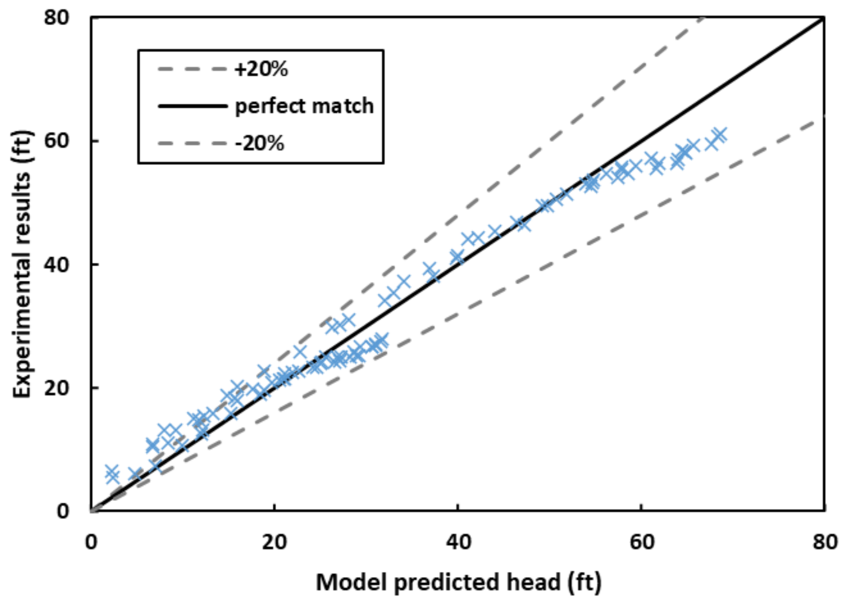

Figure 4.14 Differences between model predicted heads and experimental results for TE2700

CHAPTER 5

CONCLUSIONS AND RECOMMENDATIONS

Three methods including experimental test, numerical simulation and mechanistic modeling are used to study the viscous flow performance of ESP pumps.

5.1 Summary and Conclusions

5.1.1 Experimental study

1. Water tests are performed for the MTESP at 3600, 3000, 2400, 1800 rpm to record pump heads with corresponding flow rates. The head curve for water matches catalog head curve well. This validates the experiment setup.
2. Single-phase oil experiments are conducted using MTESP with ISO-VG320 industrial lubricate oil. The ESP boosting pressure is measured and fluid temperature is recorded. Viscosity range from 120 to 390 cP is tested at 3600 rpm and 3000 rpm. Viscosity range from 157 to 390 cP is tested at 2400 rpm. Oil viscosity is measured with viscometer for different temperatures.
3. With viscosity increase, ESP head decreases. The ESP head is also affected by fluid viscosity at low flow rate close to zero.

5.1.2 Numerical simulation

1. Single-phase water and viscous fluid CFD simulations are performed and validated with experimental results for mixed-type ESP MTESP and mixed-type ESP DN1750.

The simulation results agree with experiments, which prove the simulation setup. The CFD simulations tend to over predict the pump performance compared to the experimental results in an acceptable range.

2. Single-phase fluid viscosities from 1 to 1000 cP are simulated for both MTESP and DN1750. The pump performance behavior under viscous flow condition is analyzed. From 1 to 100 cP viscosity, pump head decreases more for MTESP than DN1750 at all operation range. Similar behavior can be found in other studies for radial pump and semi-axial pump. From 1 to 500 cP viscosity, pump head falls at low flow rate for MTESP and DN1750. Similar behaviors can be found in other studies for mixed-type pump. It can be concluded that the pump head is affected by fluid viscosity at low flow rate for mixed-type pump.

5.1.3 Mechanistic modeling

1. The previous mechanistic model is improved based on the ESP performance behavior for mixed-type pump and experimental results. The fluid viscosity and pump specific speed parameter is added in the slip factor correlation which affects the head performance. The viscous effect on turning loss is also considered in the model.
2. Pump performance catalog, water experiments and single-phase oil experiments data of three different pumps are compared with the model. The experimental results from MTESP at 3600, 3000, and 2400 rpm, DN1750 at 3500 rpm, and TE2700 at 3500 and 2400 rpm are used in this study. The pump heads predicted by the mechanistic model agree well with the experimental data for all tested pumps.

5.2 Recommendations

1. More studies about single-phase viscous flow for larger pump specific speed range need to be conducted to improve the modified slip factor in the proposed mechanistic model.
2. The experiment in this study was conducted in the winter with low ambient temperature. Additional cooling system for the test loop may be needed for doing tests at higher ambient temperatures.
3. More experimental data with higher viscosity ranges can validate and improve the proposed mechanistic model.

NOMENCLATURE

BEP	best efficiency point
BHP	brake horsepower, ML^2/T^3, kg m^2/s^3
DAQ	data acquisition system
ESP	electrical submersible pump
VSD	variable speed drive
A_{SD}	diffuser channel total wall area, L^2, m^2
A_{SI}	impeller channel total wall area, L^2, m^2
C_1	absolute fluid velocity at impeller inlet, L/T, m/s
C_{1M}	meridional velocity at impeller inlet, L/T, m/s
C_{1U}	fluid tangential velocity at impeller inlet, L/T, m/s
C_2	absolute fluid velocity at impeller outlet, L/T, m/s
C_{2B}	absolute fluid velocity at impeller outlet at Q_{bm}, L/T, m/s
C_{2E}	effective velocity at impeller outlet, L/T, m/s
C_{2F}	fluid velocity outside impeller, L/T, m/s
C_{2M}	meridional velocity at impeller outlet, L/T, m/s
C_{2P}	projected velocity, L/T, m/s
C_{2U}	fluid tangential velocity at impeller outlet, L/T, m/s
d	impeller diameter, L, m
D_C	representative impeller channel width at outlet, L, m

D_D	diffuser representative diameter, L, m
D_I	impeller representative diameter, L, m
Δ_P	differential pump boosting pressure, psi
ΔP_{total}	total pump boosting pressure, psi
ΔP_{stage}	average pump boosting pressure, psi
f	friction factor
f_{FD}	friction factor in diffuser
f_{FI}	friction factor in impeller
F_q	flowrate correction factor
f_{LK}	leakage friction coefficient
F_H	head correction factor
f_{TD}	local drag coefficient in diffuser
f_{TI}	local drag coefficient in impeller
F_γ	cross-section shape effect
F_β	pipe curvature effect
F_ω	rotational speed effect
g	gravitational acceleration
H	pump head, L, m
H_E	Euler's head, L, m
H_{EE}	effective Euler's head, L, m
H_{FD}	head loss due to friction in diffuser, L, m
H_{FI}	head loss due to friction in impeller, L, m
H_{IO}	head increase across impeller, L, m

H_R	head loss due to recirculation, L, m
H_{LK}	pressure head difference across leakage, L, m
H_{TD}	head loss due to turn in diffuser, L, m
H_{TI}	head loss due to turn in impeller, L, m
L_D	diffuser channel length, L, m
L_G	leakage channel length, L, m
L_I	impeller channel length, L, m
N	rotational speed, 1/T, rpm
Ns	specific speed
P	pressure, psi, Pa
q	volumetric flowrate, gpm
Q	volumetric flowrate, L^3/T, m^3/s, bpd
q_{bep}	flowrate at BEP, L^3/T, m^3/s
Q_{BM}	volumetric flowrate at best match point, L^3/T, m^3/s
Q_{LK}	leakage volumetric flowrate, L^3/T, m^3/s
R_1	radius of impeller inlet, L, m
R_2	radius of impeller outlet, L, m
R_D	Reynolds number by Ippen
Re	Reynolds number
Re_C	Reynolds number for recirculation effect
Re_D	Reynolds numbers in diffuser
Re_I	Reynolds numbers in impeller
Re_L	leakage Reynolds number

$Re_{Stepanoff}$	Stepanoff Reynolds number
R_{LK}	radius corresponding to leakage, L, m
S_L	leakage width, L, m
T_B	blade thickness, L, m
U_1	impeller tangential velocity at inlet, L/T, m/s
U_2	impeller tangential velocity at outlet, L/T, m/s
U_{LK}	tangential velocity due to impeller rotation at leakage, L/T, m/s
v	velocity, L/T, m/s
V_D	representative fluid velocity in diffuser, L/T, m/s
V_I	representative fluid velocity in impeller, L/T, m/s
V_L	fluid velocity at leakage, L/T, m/s
Vol_D	diffuser channel volume, L^3, m^3
Vol_I	impeller channel volume, L^3, m^3
V_S	shear velocity, L/T, m/s
W_1	relative velocity with respect to impeller at inlet, L/T, m/s
W_2	relative velocity with respect to impeller at outlet, L/T, m/s
y_{I1}	impeller inlet height, L, m
y_{I2}	impeller outlet height, L, m
Z_D	diffuser vane number
Z_I	impeller blade number

Greek Symbols

ρ	fluid density, kg/m^3

μ	fluid viscosity, Pa·s
μ_w	water viscosity, Pa·s
β	tangential blade angle, degree
σ	shear factor
σ_s	slip factor

BIBLIOGRAPHY

1. Amaral, G., Estevam, V., Franca, F.A., 2009. On the Influence of Viscosity on ESP Performance. *SPE Production & Operations*. 24(2): 303-310.
2. Amaral, G.D.L., 2007. Single-phase Flow Modeling of an ESP Operating with Viscous Fluids. MSc Thesis, State University of Campinas, Campinas, São Paulo, Brazil.
3. Ansys, 2013. ANSYS Fluent User's Guide, ANSYS, Inc. Canonsburg, PA.
4. Banjar, H., 2012. Experimental Study of Liquid Viscosity Effect on Two-Phase Stage Performance of Electric Submersible Pumps. MSc Thesis. The University of Tulsa.
5. Banjar, H., 2018. Experiments, CFD Simulation, and Modeling of Oil Viscosity and Emulsion Effects on ESP Performance. Ph.D. Dissertation. The University of Tulsa
6. Banjar, H.M., Gamboa, J., Zhang, H.-Q., 2013. Experimental Study of Liquid Viscosity Effect on Two-phase Stage Performance of Electrical Submersible Pumps. Proceedings of SPE Annual Technical Conference and Exhibition, New Orleans, Louisiana.
7. Barrios, L.J., Scott, S.L., Rivera, R., and Sheth, K.K., 2012. ESP Technology Maturation: Subsea Boosting System with High GOR and Viscous Fluid. doi:10.2118/159186-MS
8. Bing, H., Tan, L., Cao, S. and Lu, L., 2012. Prediction method of impeller performance and analysis of loss mechanism for mixed-flow pump. Science China Technological Sciences, 55(7): 1988-1998.
9. Churchill, S.W., 1977. Friction-factor Equation Spans All Fluid-flow Regimes. *Chemical Engineering* 84(24): 91-92.

10. Euler, L., 1752. Maximes pour arranger le plus avantageusement les machines destinées à elever de l'eau par moyen des pompes (Maxims for arranging most advantageously machines intended to raise water by means of pumps), *Mémoires de l'Académie Royale des Sciences et des Belles Lettres à Berlin*, 8: 185-232.

11. Euler, L., 1754. Théorie plus complette des machines qui sont mises en mouvement par la réaction de l'eau (More complete theory of machines that are set in motion by reaction with water), *Mémoires de l'Académie Royale des Sciences et des Belles Lettres à Berlin*, 10: 227-295.

12. Gamboa, J., and Prado, M., 2011. Review of Electrical-submersible-pump Surging Correlation and Models. *SPE Production & Operations*, 26(04): 314-324.

13. Gülich, J.F., 1999. Pumping Highly Viscous Fluids with Centrifugal Pumps – Part 1. World Pumps (395), 30–34.

14. Gülich, J.F., 1999. Pumping Highly Viscous Fluids with Centrifugal Pumps – Part 2. World Pumps (396), 39–42.

15. Gulich, J.F., 2007. *Centrifugal Pumps.* Berlin Heidelberg, Springer, New York.

16. Hinze, J.O., 1955. Fundamentals of the Hydrodynamic Mechanism of Splitting in Dispersion Processes. AIChE Journal, 1(3): 289-295.

17. Hole, G., 1994. Fluid Viscosity Effects on Centrifugal Pumps. Pumps and Systems, April, 1994.

18. Hydraulic Institute. 1955. Determination of Pump Performance when Handling Viscous Liquid, tenth edition.

19. Ippen, A., 1946. The Influence of Viscosity on Centrifugal Pump Performance. *Trans. ASME* 68: 823-848.

20. Li, W.G., 2000. The "Sudden-rising Head" Effect in Centrifugal Oil Pumps. World Pumps, 2000(409): 34-36.

21. Li, W.G., 2002. Experimental Investigation of Performance of Commercial Centrifugal Oil pump. World Pumps, 2002 (425), 26–28

22. Monte Verde, W., Biazussi, J., Bannwart, A., Arrifano Sassim, N., Estevam, V., 2013. Gas and Viscous Effects on the ESPs Performance. Proceedings of SPE Artificial Lift Conference-American, Cartagena, Colombia.

23. Morrison, G., Yin, W., Agarwal, R., and Patil, A., 2018. Development of Modified Affinity Law for Centrifugal Pump to Predict the Effect of Viscosity. *J. Energy Resour. Technol.* September 2018; 140(9): 092005

24. Patil, A.V., and Morrison, G.L., 2018. Affinity Laws Modified to Predict the Pump Head Performance for different Viscosities Using the Morrison Number. ASME 2018. Journal of Fluids Engineering.

25. Peng, J. 2020. Experiments and Modeling of ESP Performance with Viscous Oil and Oil-Water Emulsions. MSc Thesis. The University of Tulsa.

26. Sirino, T., Stel, H., Morales, R.E., 2013. Numerical study of the influence of viscosity on the performance of an electrical submersible pump. ASME 2013 Fluids Engineering Division Summer Meeting, American Society of Mechanical Engineers, Incline Village, Nevada, July, 2013.

27. Solano, E.A., 2009. Viscous effects on the performance of electro submersible pumps (ESP's). Master's Thesis, the University of Tulsa, Tulsa, OK.

28. Stel, H., Sirino, T., Ponce, F.J., Chiva, S., Morales, R.E.M., 2015. Numerical investigation of the flow in a multistage electric submersible pump. Journal of Petroleum Science and Engineering, 136: 41–54.

29. Stel, H., Sirino, T., Prohmann, P.R., Ponce, F., Chiva, S., Morales, R.E., 2014. CFD investigation of the effect of viscosity on a three-stage electric submersible pump. ASME 2014 4th Joint US-European Fluids Engineering Division Summer Meeting collocated with the ASME 2014 12th International Conference on Nanochannels, Microchannels, and Minichannels. American Society of Mechanical Engineers, Chicago, Illinois, August, 2014.

30. Stepanoff, A.J., 1949. How Centrifugal Pumps Perform when Pumping Viscous Oils. Power.85-87.

31. Stepanoff, A.J., 1957. Centrifugal and Axial Flow Pumps: Theory, Design and Application, 2nd Edition. New York, NY, USA: John Wiley & Sons.

32. Sun, D. and Prado, M.G., 2006. Single-phase model for electric submersible pump (ESP) head performance. SPE Journal, 11(01): 80-88.

33. Thin, K.C., Khaing, M.M. and Aye, K.M., 2008. Design and performance analysis of centrifugal pump. World Academy of Science, Engineering and Technology, 46: 422-429.

34. Trevisan, F., Prado, M., 2011. Experimental investigation of the viscous effect on two-phase-flow patterns and hydraulic performance of electrical submersible pumps. Journal of Canadian Petroleum Technology. 50 (4): 45–52.

35. Vieira, T.S., Siqueira, J.R., Bueno, A.D., Morales, R.E.M., and Estevam, V., 2015. Analytical study of pressure losses and fluid viscosity effects on pump performance during monophase flow inside an ESP stage. Journal of Petroleum Science and Engineering, 127(2015): 245-258.

36. Wiesner, F.J., 1967. A review of slip factors off centrifugal impeller. J. Eng. Power, 89(4), 558-566.

37. Zhang, J., 2017. Experiments, CFD Simulation, and Modeling of ESP Performance under Viscous Fluid Flow Conditions. MSc Thesis. The University of Tulsa.

38. Zhu, J., Banjar, H., Xia, Z., and Zhang, H.-Q., 2016. CFD Simulation and Experimental Study of Oil Viscosity Effect on Multi-stage Electrical Submersible Pump (ESP) Performance. Journal of Petroleum Science and Engineering, 146, 735-745.

39. Zhu, J., Guo, X., Liang, F., and Zhang, H.-Q., 2017. Experimental Study and Mechanistic Modeling of Pressure Surging in Electrical Submersible Pump. Journal of Natural Gas Science and Engineering, 45: 625-636.

40. Zhu, J., Zhu, H., Cao, G., Banjar, H., Peng, J., Zhao, Q., and Zhang, H.-Q., 2019. A New Mechanistic Model for Oil-Water Emulsion Rheology and Boosting Pressure Prediction in Electrical Submersible Pumps ESP. doi:10.2118/196155-MS

41. Zhu, J., Zhu, H., Cao, G., Zhang, J., Peng, J., Banjar, H. and Zhang, H.Q., 2020. A New Mechanistic Model to Predict Boosting Pressure of Electrical Submersible Pumps Under High-Viscosity Fluid Flow with Validations by Experimental Data. SPE Journal, 25(02), pp.744-758.

42. Zhu, J., Zhao, H., Cao, G., Banjar, H., Zhu, H., Peng, J. and Zhang, H.Q., 2021. A New Mechanistic Model for Emulsion Rheology and Boosting Pressure Prediction in Electrical Submersible Pumps (ESPs) under Oil-Water Two-Phase Flow. SPE Journal, pp.1-18.

43. Zhu, H., Zhu, J., Lin, Z., Zhao, Q., Rutter, R., & Zhang, H. Q. 2021. Performance degradation and wearing of Electrical Submersible Pump (ESP) with gas-liquid-solid flow:

Experiments and mechanistic modeling. Journal of Petroleum Science and Engineering, doi: 10.1016/j.petrol.2021.108399

44. Zhu, J. 2017. Experiments, CFD Simulation and Modeling of ESP Performance Under Gassy Conditions. Ph.D. Thesis. The University of Tulsa.

45. Zhu, H. 2019. Experiments, CFD Simulation and Modeling of Sand Wear and Performance Degradation in ESPs. Ph.D. Thesis. The University of Tulsa.

APPENDIX A

EQUIPMENT AND INSTRUMENT SPECIFICATIONS

Table A.1 Experimental equipment list

Equipment/Instrument	Model	Capacity/Range
ESP pump	MTESP	BEP: 3100 bpd, 3500 rpm
Electric motor	WEG 05036EG3E326TS-W22	50 hp
Variable speed drive	FUJI ELECTRIC FRN050G1S-4U	50 hp, 380 ~ 480 V, 70 A
ESP thrust chamber	HSG, Thrust chamber 1.x series horizontal	–
Air compressor	Kaeser CSD60	186 cfm, 217 psi
Liquid control valve	Manually gate valve	–
Gas control valve	Emerson 24588SB	–
Temperature transmitter	INOR IPAQ R330	-50-200^{o}C
Absolute pressure transmitter	Endress Hauser PMC71	6 ~ 600 psig
Differential pressure transmitter	Endress Hauser PMD75	0.45-45 psig
Coriolis liquid flowmeter	Endress Hauser Promass 80F	0 ~ 10000 bpd
Proximity probe	GE 3300 NSV	10-90 mils
Proximitor	GE 3300 XL NSV	Output: 200 mV/mil, 100 KHz
Pressure regulator	NORGREN 1/2" NPT Regulator	10-250 psig, 212 cfm
POP safety valve	APOLLO Bronze POP safety valve	400 psig
Torque sensor	S.Himmelstein MCRT28004T(5-3)NFA	0 ~ 8500 rpm 0 ~ 5000 lbf-in
Torque sensor monitor	S.Himmelstein model 721	2000 samples/sec

Table A.2 Data acquisition system specifications

Equipment/Instrument	Model	Capacity/Range
Fieldpoint chassis	NI cFP-1804	–
Fieldpoint analog input	NI cFP-AI-111	16 channels; input ranges 0-20 mA/4-20 mA ±20 mA; updating rate 0.83-3 Hz
Fieldpoint output	NI cFP-AO-200	8 channels, current output, 200 Hz
Fieldpoint voltage input	NI cFP-AI-100	8 channels; input range ±1V, ±5V, ±15V, ±30V, 0-1V. 0-5V, 0-15V, 0-30V, 0-20 mA/4-20 mA ±20 mA; updating rate 360 Hz
Fieldpoint supply	NI cFP-CB-1	–
CompactDAQ analog output	NI 9265	0 to 20mA, 16-Bit, 100 kS/s, 4-Ch AO module
CompactDAQ voltage input	NI 9228	8-Ch +/-60 V, 1 kS/s/ch, 24-Bit, Ch-to-Ch Isolated AI module
CompactDAQ chassis	NI 9939	Backshell for 16-pos connector block (qty 1)
CompactDAQ analog input	NI 9208	24-bit current input module with D-Sub
CompactDAQ chassis	NI 9923	Front-mount terminal block for 37-pin D-Sub Modules
Power supply	AutomationDirect	–
Terminal blocks	AutomationDirect	–
Circuit protection blocks	AutomationDirect	–
Konnect-It terminal block jumper	AutomationDirect	–
Electrical enclosure	Hoffman	–
Computer	Dell	–
Terminals tubular cable lug	YONGCUN	–

Figure A.1 Liquid flow control valve

Figure A.2 Temperature sensor

Figure A.3 Water tank

Figure A.4 Coriolis liquid flowmeter

Figure A.5 Pressure regulator

Figure A.6 Air compressor

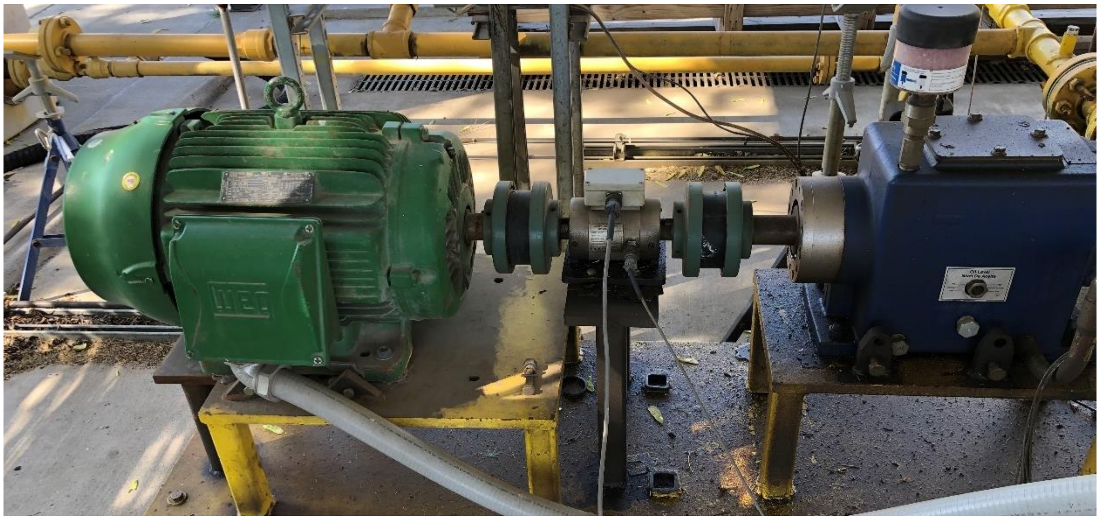

Figure A.7 Electric motor

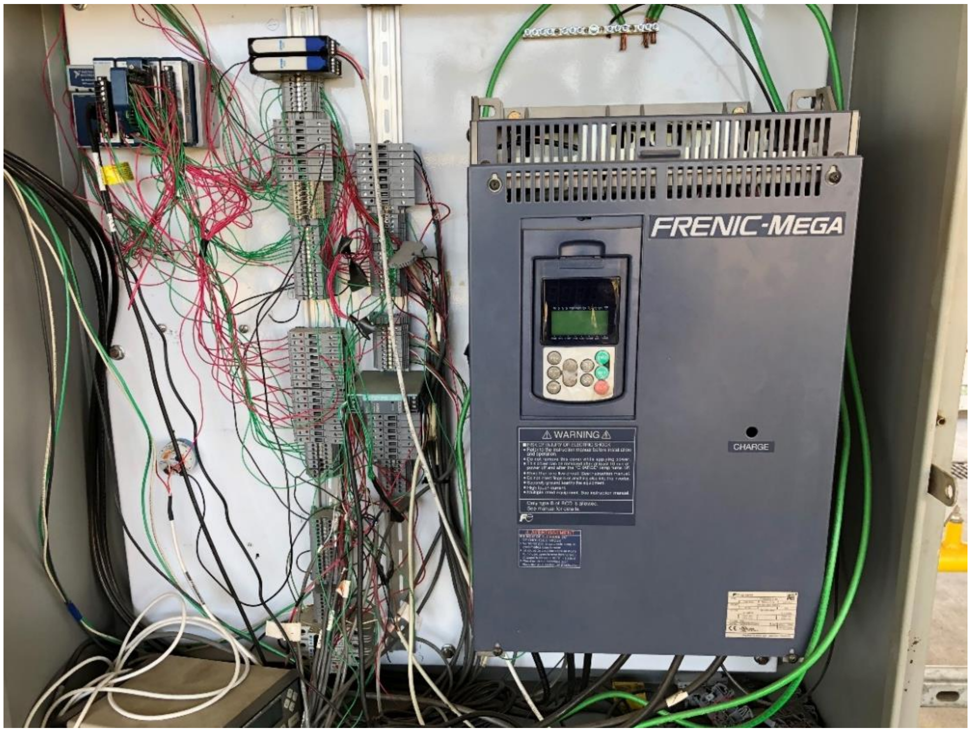

Figure A.8 Data acquisition devices and VSD

Figure A.9 Rotational rheometer

APPENDIX B

MECHANISTIC MODEL FLOWCHART

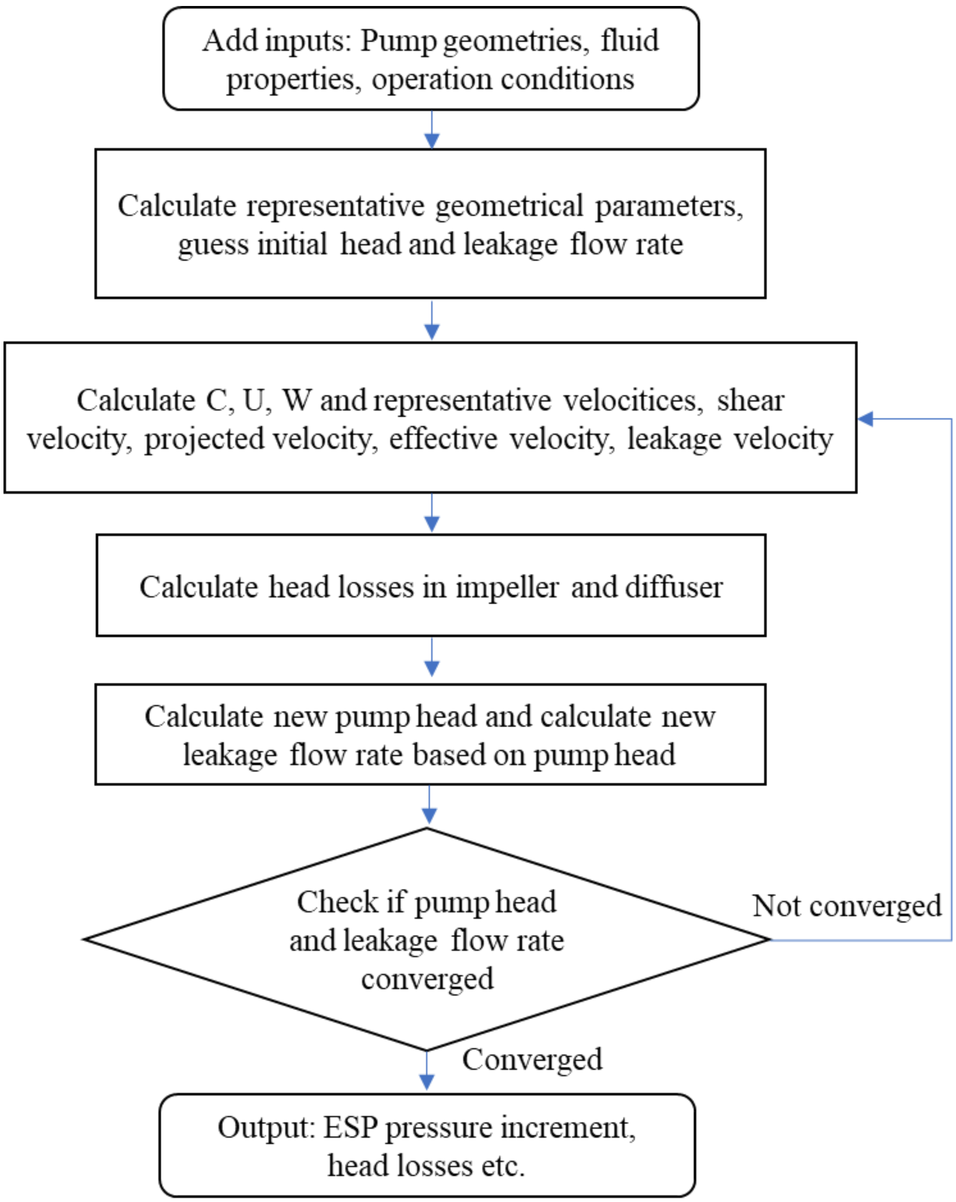

Figure B.1 Flow chart of mechanistic model